Characterization of iron oxides in mineral dust aerosols: Implications for light absorption

Sandra Lafon,[1] Irina N. Sokolik,[1] Jean Louis Rajot,[2] Sandrine Caquineau,[3] and Annie Gaudichet[4]

Received 20 December 2005; revised 28 March 2006; accepted 26 May 2006; published 8 November 2006.

[1] We report on measurements that were specifically designed to determine iron oxides in mineral dust aerosols needed for improved optical modeling. Atmospheric dust samples as well as samples generated in a wind tunnel from soils were analyzed by a number of analytical techniques for their total and free iron content (bulk and size resolved), hematite and goethite, mineralogy, and size distribution. These samples are representative of several important dust sources in East Asia and northern Africa. A novel data set generated from these measurements enables us to perform an in-depth modeling study of dust optical properties in the solar spectrum. We modeled the iron oxide–clay aggregates, which are the key light-absorbing species, as well as their mixtures with nonabsorbing minerals. A volume fraction of iron oxide in aggregates was determined from measurements. Significant differences in the single-scattering albedo, ω_0, were found between hematite- and goethite-clay aggregates, although these calculations involved several important assumptions about the partition of hematite and goethite in size-resolved aggregates. Furthermore, we found that variability of the free iron content is large enough to cause important differences in ω_0 of mineral dust originating from different sources. In contrast, this variability has little effect on the extinction coefficient and optical depth. We demonstrate that for the same size distribution, ω_0 calculated from data obtained for Chinese and Tunisian samples show higher values and more distinct wavelength dependence than those of Niger dust. All the above ω_0 differ from ones calculated using the refractive indices of Patterson et al. (1977) or the OPAC model (Hess et al., 1998), which are often used in radiative transfer studies. We conclude that information on a size-resolved content of free iron and a fraction of hematite and goethite in aggregates will need to be known on a regional basis to improve the prediction of the single-scattering albedo at solar wavelengths and hence the radiative impact of atmospheric mineral dust.

Citation: Lafon, S., I. N. Sokolik, J. L. Rajot, S. Caquineau, and A. Gaudichet (2006), Characterization of iron oxides in mineral dust aerosols: Implications for light absorption, *J. Geophys. Res.*, *111*, D21207, doi:10.1029/2005JD007016.

1. Introduction

[2] During the last decade, there has been a considerable interest in studying the radiative effects of atmospheric mineral dust, especially its ability to absorb sunlight. An understanding of how much dust particles can absorb is central to many problems of atmospheric sciences ranging from photochemistry and photosynthesis to climate change [*Sokolik et al.*, 2001]. Optical properties of dust are also needed for the interpretation of both ground-based and satellite remote sensing observations. Although several quantities can be used for characterizing how absorbing dust is (such as the imaginary part of the refractive index or absorption coefficient), the single-scattering albedo ω_0 is the most common parameter cited in the literature. Examining ω_0 reported for dust in the solar spectrum, one finds a wide range of values. Some recent studies based on satellite and/or AERONET retrievals reported ω_0 as high as 0.95–0.99 in midvisible concluding that dust has low absorption [*Kaufman et al.*, 2001; *Dubovik et al.*, 2002]. On the basis of in situ measurements of scattering and absorption coefficients conducted from the NCAR C-130 aircraft during the ACE-Asia field experiment, *Anderson et al.* [2003] found ω_0 of 0.96 (±0.01) at 550 nm for dust particles in the coarse size mode (aerodynamic-equivalent diameter is higher than 1 μm). Conversely, studies that modeled ω_0 using the refractive index of *Patterson et al*. [1977] reported much lower ω_0 values. The latter is in agreement with ω_0 from *World Climate Program* [1983], *d'Almeida et al.* [1991] as well as OPAC models [*Hess et al.*, 1998]. Prior studies have already pointed out that the existing range of ω_0 is large

[1] School of Earth and Atmospheric Sciences, Georgia Institute of Technology, Atlanta, Georgia, USA.
[2] Institut de Recherche pour le Développement, UR 049, Niamey, Niger.
[3] Institut de Recherche pour le Développement, UR Paleotropique, Bondy, France.
[4] Laboratoire Interuniversitaire des Systèmes Atmosphériques, UMR CNRS 7583, Universités Paris 7 et Paris 12, Créteil, France.

0148-0227/06/2005JD007016

Table 1. Summary of Atmospheric and Laboratory-Generated Dust Samples Analyzed in This Study

Sample	Abbreviation	Collect Location	Sampling Time Period	Number of Analyzed Samples	Transport Distance
		Atmospheric Samples			
Niger, Harmattan	Ni-Ha	Sahel, 13°31′N, 2°38′E	Feb 1996–1998	nine bulk filters	midrange
Niger, local erosion	Ni-LE	Sahel, 13°31′N, 2°38′E	Feb 1996–1998	seven bulk filters	source
China, Zhenbeitai	Ch-ZBT	China, 38°17′N, 109°43′E	Apr 2002	four bulk filters	midrange
Cape Verde, Sahel	CV-Sl	Cape Verde, 16°45′N, 22°57′W	Jan 1992	three bulk filters	long range
Cape Verde, south Morocco	CV-SM	Cape Verde, 16°45′N, 22°57′W	Jan 1993	three bulk filters	long range
Cape Verde, central Sahara	CV-CS	Cape Verde, 16°45′N, 22°57′W	Feb 1994	three bulk filters	long range
		Generated Samples			
Niger, wind tunnel	Ni-WT	Sahel, 13°31′N, 2°38′E	generated in laboratory from soil	three bulk filters; two impactors	source
Tunisia, wind tunnel	Tu-WT	North Sahara, 33°01′N, 10°40′E	generated in laboratory from soil	three bulk filters; one impactor	source
China, wind tunnel	Ch-WT	China, 39°26′N, 105°40′E	generated in laboratory from soil	three bulk filters; two impactors	source

enough to cause either positive or negative direct radiative forcing [*Sokolik and Toon*, 1996; *Intergovernmental Panel on Climate Change*, 2001]. Given the importance of the subject, a better understanding of the nature of light absorption by dust particles is urgently needed.

[3] It has been recognized that optical properties of dust aerosol particles are controlled by their physicochemical characteristics. *Sokolik and Toon* [1999] proposed a technique to model optical properties of mineral aerosols which accounts for their composition. The technique considers dust as an external mixture of individual minerals and their aggregates. It has been demonstrated that the abundance of iron oxide–clay aggregates is a key factor controlling the light absorption of dust at solar wavelengths [*Sokolik and Toon*, 1999]. However, their study was hampered by a lack of data on size-resolved mineralogical composition of atmospheric dust required for such a modeling. The need for new data, especially as a function of size and on a regional basis, provided motivation for our study. Here we present the results of measurements that, for the first time, were specifically carried out to provide information on physicochemical characteristics of regional dust aerosols needed for modeling of their optical properties. In particular, this paper, which is the first of a series, reports new data on iron oxide characteristics along with a new approach for incorporating this data into optical modeling.

[4] Our study addresses several key problems. First, it is important to determine the fraction of iron that is involved in iron oxides (called free iron). Unlike structural iron, which is a common substitution ion in the aluminosilicate crystal lattice, free iron is responsible for light absorption [e.g., *Sherman and Waite*, 1985; *Jepson*, 1988]. To this end, we benefit from a new technique developed by *Lafon et al.* [2004] to measure the free iron amount in aerosol samples. Second, recent studies demonstrated that iron oxides in atmospheric mineral aerosols occur either as hematite or goethite [*Arimoto et al.*, 2002]. Thus information on the relative abundance of these species in regional samples is needed to investigate how dust optical properties can be affected by mineralogy of iron oxides. This is an important issue since the *Sokolik and Toon* [1999] study as well as several others considered only hematite in optics modeling mainly due to a lack of data on goethite. Third, given that dust is a mixture of various species and that iron oxides are mainly associated with clays in the form of aggregates, the relative abundance of iron oxide–clay aggregates and nonabsorbing minerals is clearly important. To address this problem, we develop an approach for constructing the composition of aggregates and their mixtures with other minerals based on measurements of iron oxide characteristics and mineralogy. Both bulk and size-resolved data were obtained and used in optical modeling to refine the methodology for measuring characteristics of dust aerosols needed in radiative transfer studies.

[5] This paper is organized as follows. Section 2 describes dust samples and analytical methods used for their analysis. This section also introduces our approach to modeling the optical properties of iron oxide–clay aggregates and their mixtures with other minerals. Then section 3 presents the results of physicochemical characterization of dust aerosols focusing on the iron oxide properties such as free and total iron, mineralogy, and bulk and size-segregated content of iron oxides in aerosol and soil samples. The results of optical modeling based on Mie theory and data obtained in this study are presented and discussed in section 4. Section 5 summarizes our major findings.

2. Methodological Approach

2.1. Dust Samples

[6] Two types of aerosol samples are analyzed in this study: atmospheric dust samples and samples of laboratory-generated dust aerosols. The atmospheric dust samples were collected in Northern Africa and East Asia during several field campaigns under the dust-laden conditions. The laboratory-generated dust aerosols were produced from natural Tunisian, Chinese and Nigerian soil samples using a wind tunnel system [*Alfaro and Gomes*, 1995]. This system enables one to reproduce in well-controlled laboratory settings the complex processes of saltation/sandblasting that are responsible for mineral dust emission in natural conditions [e.g., *Alfaro and Gomes*, 2001].

[7] Table 1 introduces all analyzed samples, providing information on their aging, and time and location of sample collection. They are classified as source, midrange trans-

ported, and long-range transported aerosols. The source samples are representative of freshly emitted dust in a particular source region, including dust from local erosion events and dust aerosols generated in the laboratory. Generating aerosols in the laboratory is a convenient way to produce pure desert aerosols representative of an individual source. Midrange transported aerosols are those collected in desert areas but at some distance from the source (or multiple sources), whereas long-range transported dust are those found at the great distances from the source region. The latter dust particles are likely to undergo aging via a number of physical and chemical processes. Thus aging is an important factor that needs to be taken into account in comparing bulk and size-resolved physicochemical properties of dust samples.

[8] Table 1 also gives the number of bulk and impactor-collected samples used in our study for each dust type. All atmospheric dust samples were collected on the 0.4 μm pore polycarbonate filters at about 10 m above the surface. Sample collection was performed between 15 and 150 min in Sahel and China and during 24 hours in Cape Verde.

[9] Two different dust events were sampled at the same Sahel site, Banizoumbou (13°31′N, 2°38′E) near Niamey, Niger. The Niger local erosion samples (hereinafter referred to as Ni-LE) were collected in spring during dust storms that originated from local erosion [*Rajot*, 2001]. Therefore Ni-LE samples are representative of this particular source. In contrast, Niger Harmattan samples (hereinafter referred to as Ni-Ha) were collected in the winter when wind blew from the Sahara bringing dust mainly from the Chad basin [*Herrmann et al.*, 1999]. The potential sources of this midrange transported dust are within the Chad basin as well as other source regions along the transport route. Chinese dust samples were collected in Zhenbeitai (38°17′N, 109°43′E). This site is located downwind of the Gobi Desert [*Alfaro et al.*, 2003], so these samples (hereinafter referred to as Ch-ZBT) are representative of midrange transported dust. Owing to high concentrations of local pollution, contamination of dust samples is highly likely. To avoid this problem, here we analyzed samples that were collected during the strong dust events when concentrations of dust particles were much larger compared to other aerosols. The samples collected at Cape Verde, Sal Island (16°45′N, 22°57′W), are representative of long-range transported Saharan dust. They have been classified according to their region of origin based on both back-trajectories analysis and their mineralogy [*Chiapello et al.*, 1997; *Caquineau et al.*, 2002]. These samples were collected during several dust events originating in the Sahel, south of Morocco, and central Sahara.

[10] Three different natural soil samples were used to generate dust aerosols in the wind tunnel system. Only the first centimeter of the soil surface, consisting of loose grains prone to wind erosion, has been collected in three different dust source regions: Niger, Banizoumbou site (13°31′N, 2°38′E), near Niamey; Tunisia, Maouna site (33°01′N, 10°40′E), near Tataouine, and China, Ulan Buh area (39°26′N, 105°40′E). All these soils are sandy soil types but have different mineralogical composition as discussed below.

[11] The soil samples were analyzed with a number of analytical techniques in order to explore the linkage between their properties and properties of dust aerosols generated from them, especially the content of iron oxides. Soil samples were crushed and suspended in filtered ethanol in order to prepare a filter of bulk soil that could be analyzed in a way similar to aerosol samples. For that, the suspension of soil particles was filtered on the 0.4 μm pore polycarbonate filter. Three filters of each soil were prepared for analysis. We also analyzed the clay size fraction (less than 2 μm particles) and the fine silt fraction (2 to 20 μm) that were separated by using a liquid sedimentation method. These two size fractions are of particular interest to our study because soil particles in this size range potentially could become dust aerosols during the emission processes. However, one cannot expect to find one-to-one relations between soil particles in clay and silt fractions and atmospheric dust particles. Emission processes result only in partial destruction of soil aggregates, whereas the liquid separation technique, which is a classical way to characterize fine soil particles, causes their complete disaggregation. Although measurements made on clay and fine silt soil fractions cannot be used directly to infer information on dust aerosols, they are useful in studying the linkage between dust aerosols and their parent soil. The separation of clay and fine silt fractions of soil particles was made with the sedimentation technique based on the Robinson pipette method in deionized water [*Baize*, 2000]. H_2O_2 was used to remove organic mater of the soil which is an aggregating agent, and to avoid bacterial growth that might lead to a flocculation process. The suspensions of the clay fraction and fine silt fraction were then filtered on the 0.4 μm pore polycarbonate membrane. Three filters were prepared from each suspension.

[12] The aerosols generated from soils with the wind tunnel system were collected with an original device called the isokinetic particle collector (IPC) described by *Alfaro et al.* [2004]. The IPC consists of a sedimentor and a collecting chamber. An isokinetic inlet, with the diameter adjusting to the wind speed in the wind tunnel, feeds the flow into the IPC. Having the sedimentor with a size cut off of 30 μm, this system collects only an aerosol size fraction of the generated samples, excluding large saltating particles. The collecting chamber includes several tubes which enable one to perform isokinetic collection of a homogenous sample simultaneously for several instruments. Both bulk samples on the polycarbonate filter and cascade impactor samples of generated dust aerosols were collected using this system. The bulk samples were collected onto 0.4 μm pore polycarbonate filters for 1–4 min. Size- resolved samples were collected with a Dekati low-pressure multijets cascade impactor with a flow rate of 30 L/min for about 1.5–3 min. The impactor has 13 stages with 50% cut points (d_{50}) of 0.03, 0.06, 0.10, 0.17, 0.26, 0.40, 0.64, 1.00, 1.62, 2.47, 4.00, 6.62, and 10.24 μm. To avoid bounce and disaggregation of particles, the surface of impactor stage plates was coated with grease made of vaseline dissolved in cyclohexane (4% mass dilution). Coated plates were air dried before particle collection. After collection, plates were rinsed with cyclohexane and the suspension was filtered onto a polycarbonate membrane. Mass of dust aerosols collected on the finest stages during the wind tunnel experiment was too low to perform the size-segregated analysis. Therefore the six

finest stages were combined together on a filter and considered as one size bin below 0.4 μm. Thus eight impactor stages were available for the analysis of size-resolved elemental mass.

2.2. Analytical Methods

[13] Several methods have been utilized in this study to perform qualitative and quantitative characterizations of iron oxides in the samples and to obtain size-resolved information. We used X-ray Fluorescence (XRF) Spectrometry for the elemental analysis; an aerosol-adapted chemical method based on citrate-bicarbonate-dithionite (CBD) reagent for quantification of iron oxides; and diffuse reflectance spectroscopy (DRS) for mineralogical speciation of iron oxides. For each aerosol type, several filters were collected in order to obtain the amount of material required for different analyses.

2.2.1. XRF Spectrometry

[14] Using this technique, elemental analysis was carried out for all samples. The method is nondestructive and quantitative for elements with atomic number 10 or higher [*Elichegaray et al.*, 1981]. Analysis was performed directly on the filters using a Philips PW2404 4 kW spectrometer equipped with a rhodium tube. The blank polycarbonate filters were also analyzed for each sampling series. For the filters used in this study, detection limits varied between 0.005 and 0.15 μg, and quantification thresholds ranged from 0.02 to 0.5 μg. The results were expressed in terms of element oxide mass, which is a common approach for characterizing the minerals: Na_2O, MgO, Al_2O_3, SiO_2, P_2O_5, SO_3, K_2O, CaO, MnO, TiO_2, and Fe_2O_3. We then calculated the percentage of each element oxide in the total mass, which was obtained by summing up all oxides considered. The final results are the mean values and their standard deviations computed for all the filters collected for a given type of dust aerosols.

2.2.2. Aerosol-Adapted CBD Method

[15] Following *Lafon et al.* [2004], samples were treated with CBD to determine the free iron content. This method is an adaptation for aerosol filters (with typical material mass less than 500 μg) of the classical method developed originally by *Mehra and Jackson* [1960] for soil analysis. The method uses the CBD reagent to dissolve free iron oxides selectively via reduction. The remaining iron, called structural iron, occurs in the crystal lattice of silicates and does not contribute to the absorption of visible light [*Faye*, 1968; *Karickhoff and Bailey*, 1973].

[16] Free iron quantification was performed for at least three filters for each dust sample, including both atmospheric and wind tunnel bulk samples, as well as for wind tunnel impactor stages, after they have been transferred to the filters, provided that there was enough mass of material.

2.2.3. Diffuse Reflectance Spectroscopy (DRS)

[17] To discriminate between hematite and goethite, we employed diffuse reflectance spectroscopy (DRS). Previously, *Arimoto et al.* [2002] showed that this method is capable of discriminating hematite from goethite in dust samples with concentrations typical of those of atmospheric filters. This speciation cannot be provided by usual mineralogical (X-ray diffraction) or elemental composition analytical methods. DRS uses the characteristic bands of hematite and goethite in the visible absorption spectrum at around 565 nm and 435 nm, respectively. Moreover, by taking the second derivative of the diffuse reflectance signal, it is possible to determine quantitatively a relative mass fraction of hematite and goethite [*Scheinost et al.*, 1998].

[18] Dust aerosol samples were transferred from the polycarbonate filters to a white Teflon plate. This was a required step to enable measurements with low aerosol amounts. The procedure was performed on three types of dust aerosol samples: Ch-ZBT, Ni-WT, and Tu-WT. Measurements were carried out at room temperature with a Cary 5G UV-VIS-NIR spectrophotometer equipped with a 110-mm-diameter integrating sphere coated with Halon (Labsphere, Inc.). Analyses were performed for spectra in the range from 350 to 1200 nm with a step of 0.5 nm. Reflectance, R, was measured relative to a Halon standard. The remission function $f(R) = (1 - R^2)/R$, proportional to the concentration of absorber, was calculated according to the Kubelka-Munk relation. The nature and relative proportion of the iron oxides were determined from the position and intensity of absorption bands of second derivative curves calculated from $f(R)$ [*Scheinost et al.*, 1998]. The amplitudes of the $^6A_1 \rightarrow {}^4E$ transition band (A_{goet}) and the electron pair transition band (A_{hem}) are commonly used to assess the contents of goethite and hematite, respectively. The relative proportion of hematite in iron oxide mass is estimated from the calculated ratio $A_{hem}/(A_{hem} + A_{goet})$. By combining this method and the CBD method, we were able to quantify the mass fraction of hematite and goethite, unlike the study of *Arimoto et al.* [2002] that reported only the presence of these species.

2.3. Modeling Approach

[19] In order to investigate how iron oxide characteristics can affect optical properties, we performed extensive calculations of the light extinction coefficient and single-scattering albedo by considering the range of the iron oxide content and mineralogy determined in bulk and size-resolved measurements. In this study we rely on Mie theory calculations assuming that dust particles are spherical. The effect of particle nonsphericity will be addressed in a following paper.

[20] The size distribution required for Mie calculations was constrained by using impactor measurements. The impactor provides the particle mass size distribution (MSD) as a function of aerodynamic equivalent diameter. Size distributions consisting of two size modes were considered. Each size mode was approximated by a lognormal function with a median diameter d_{0m} and dispersion σ (geometric standard deviation) as

$$\frac{dM}{d\ln d} = \frac{M_0}{\sqrt{2\pi}\ln\sigma}\exp\left(-\frac{(\ln(d/d_{0m}))^2}{2\ln^2\sigma}\right), \quad (1)$$

where M_0 is the particle mass concentration of a given size mode. The particle mass of each size mode and the parameters of its lognormal distribution were estimated from measured MSD following *Gomes et al.* [1990] as described in section 3.1. Then for each size mode the

parameters of the particle number size distribution were calculated as [*Seinfeld and Pandis*, 1998]

$$\sigma_n = \sigma_m = \sigma, \tag{2}$$

$$d_{0n} = \exp\left(\ln(d_{0m}) - 3\ln^2\sigma\right), \tag{3}$$

$$N_0 = M_0 / \left(\frac{\pi}{6\rho \times d_{0m}^3}\right), \tag{4}$$

where subscripts n and m denote the parameters of the particle number and mass distributions, respectively, N_0 is the particle number concentration of a given mode, and ρ is the particle density, which is assumed here to be 2.5 g/cm^3.

[21] In addition to the particle size distribution, Mie calculations require information on the mineralogical composition of a dust mixture since individual minerals as well as their aggregates each have a specific spectral refractive index [*Sokolik and Toon*, 1999]. Here we consider the dust mixtures consisting of two nonabsorbing species (quartz (SiO_2), calcite ($CaCO_3$)), and iron oxide–clay aggregates. Association of iron oxides with clay has been well documented in the soil science literature [e.g., *Sumner*, 1963; *Greenland et al.*, 1968]. We assume that clay minerals can be either illite $(K_{0.7},Na_{0.2},Ca_{0.1})(Al_3,Fe_{0.6},Mg_{0.4})(Si_7,Al)O_{20}(OH)_4$ [*Caquineau*, 1997] or kaolinite $Al_4[Si_4O_{10}](OH)_8$ [*Deer et al.*, 1992]. Iron oxides were considered as hematite (Fe_2O_3) and goethite (FeOOH). The above assumption of the external mixture consisting only of three types of species is an important simplification, because dust is the mixture of many different minerals. However, it is justified for this study since our main focus here is on light absorption of dust. Although simplified, these mixtures enable us to take into account both light nonabsorbing species (such as quartz and calcite) and light-absorbing iron oxide–clay aggregates. We selected quartz and calcite to represent the nonabsorbing mineral species for several reasons. Quartz is the major nonclay species in all mineral dust [*Glaccum and Prospero*, 1980]. Unlike quartz, calcium carbonates are more variable depending on parent desert soils. Thus having calcium carbonate in the dust mixture allows us to account for the varying amount of nonabsorbing species. Illite and kaolinite were chosen to represent the clay component because they are the most common type of clays measured in atmospheric mineral dust. Illite is an ubiquitous specie, and it has been found to be the major clay in mineral dust aerosols originating from the Sahara [*Chester et al.*, 1977] and from the Asian continent [*Merrill et al.*, 1994]. In turn, kaolinite varies from source to source, being the major clay in dust originating in the Sahel [*Chester et al.*, 1972; *Caquineau et al.*, 1998].

[22] To carry out optical modeling, we need to know a particle number fraction of quartz, N_{qzt}, calcite, N_{cal}, and iron oxide–clay aggregates, N_{agg}, in each size mode. This information was obtained from the data of elemental analysis performed on impactor and bulk samples (see section 3.2). For each size mode, the relative proportions (in terms of the particle number) of quartz (abbreviated as qzt), calcite (cal), and iron oxide–clay aggregates (agg) were calculated as

$$N_{agg} = \frac{m_{Al}}{f_{Al-clay} \times \rho_{clay}\left(4/3\pi r_{0n}^3 \exp\left(9\ln(\sigma)^2/2\right)\right)}, \tag{5}$$

$$N_{cal} = \frac{m_{Al} \times \left(Ca/Al\right)_{spl}}{f_{Ca-cal} \times \rho_{cal}\left(4/3\pi r_{0n}^3 \exp\left(9\ln(\sigma)^2/2\right)\right)}, \tag{6}$$

$$N_{qtz} = \frac{m_{Al}\left(\left(Si/Al\right)_{spl} - \left(Si/Al\right)_{clay}\right)}{f_{Si-qtz} \times \rho_{qtz}\left(4/3\pi r_{0n}^3 \exp\left(9\ln(\sigma)^2/2\right)\right)}, \tag{7}$$

where ρ_{clay}, ρ_{cal}, and ρ_{qzt} are the density of clay, calcite, and quartz, respectively; $f_{Al\text{-}clay}$, $f_{Ca\text{-}cal}$, and $f_{Si\text{-}qzt}$ are the molar mass fraction of aluminum in clay, calcium in calcite and silicon in quartz, respectively; m_{Al} is the mass of aluminum measured in the dust sample, $4/3(\pi r_{0n}^3)\exp(9\ln(\sigma)^2/2)$ is the volume of particles having the lognormal size distribution with the median radius r_{0n} and dispersion σ, and $(Ca/Al)_{spl}$, $(Si/Al)_{spl}$, and $(Si/Al)_{clay}$ are the mass elemental ratio of calcium and silicon to aluminum in samples (spl) or in the clay mineral formulae (clay), respectively. In equations (5)–(7) it is assumed that all Al is involved in clay particles, all Ca is involved in calcium carbonate (considered as calcite), and Si is involved in both quartz and clay particles.

[23] We also need to know a volume fraction, ν, of iron oxide in the iron oxide–clay aggregates. The volume fraction was calculated from the Fe/Al mass ratio by assuming that all Al is involved in a particular clay species, and that the partition of iron oxides is homogeneous among clay particles (i.e., in each size mode, all iron oxide–clay aggregates have the same ν). Then ν can be found as

$$\nu = \frac{\left(\frac{V_{FeOx}}{V_{clay}}\right)}{1 + \left(\frac{V_{FeOx}}{V_{clay}}\right)}, \tag{8}$$

where V_{FeOx}/V_{clay} is the volume ratio of iron oxide and clay. The latter can be found using the Fe/Al ratio as

$$\frac{V_{FeOx}}{V_{clay}} = \frac{Fe}{Al} \times \frac{f_{Al-clay}}{f_{Fe-FeOx}} \times \frac{\rho_{clay}}{\rho_{FeOx}}, \tag{9}$$

where ρ_{clay} and ρ_{FeOx} are the density of clay and iron oxides, and $f_{Al\text{-}clay}$ and $f_{Fe\text{-}FeOx}$ are the molar mass fractions of aluminum in clay and iron in iron oxide, respectively. Thus ν depends on both the mineralogy of iron oxides and clays forming a particular iron oxide–clay aggregate.

[24] Having ν, the effective refractive indices of aggregates were computed with the Bruggeman approximation following *Sokolik and Toon* [1999]. Spectral refractive indices of quartz, calcite, kaolinite, illite, and hematite are available in the solar spectrum from 200 to 1000 nm [*Sokolik and Toon*, 1999]. The refractive index of goethite was reported by *Bedidi and Cervelle* [1993] in the range from 460 to 700 nm.

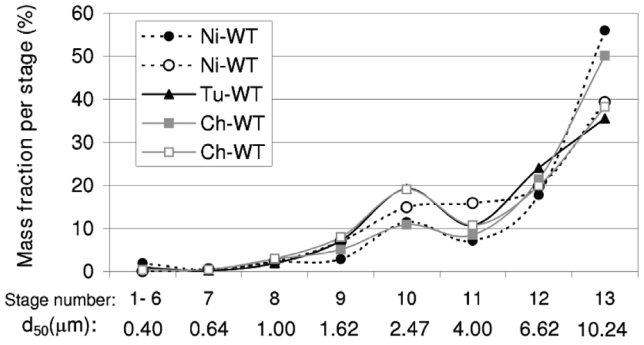

Figure 1. Mass size fraction (%) measured on impactor stages for two Niger wind tunnel samples, two Chinese wind tunnel samples, and one Tunisia wind tunnel sample. The x axis shows the stage number and size cut diameters (d_{50}). The y axis is the percentage of the total mass (defined as the sum of all analyzed elements in their oxide forms).

[25] In the case of the external mixture of three species (quartz, calcite, and iron oxide–clay aggregates) having two size modes, the extinction coefficient (or scattering coefficient) can be calculated as a weighted sum of the extinction coefficients (or scattering coefficients) of individual species in each size mode:

$$K^*_{\text{ext}} = \sum_{i=1,2} N_i \left(N_{\text{qzt,i}} K^*_{\text{ext,qzt,i}} + N_{\text{cal,i}} K^*_{\text{ext,cal,i}} + N_{\text{agg,i}} K^*_{\text{ext,agg,i}} \right), \quad (10)$$

where K^*_{ext} is the normalized extinction coefficient (or normalized scattering coefficient, K^*_{sc}) (here normalized means for the particle number concentration of 1 cm^{-3}), N_i is the relative fraction of the ith mode, $N_{\text{qzt,i}}$, $N_{\text{cal,i}}$, and $N_{\text{agg,i}}$ are the relative fractions of the particle number concentration of quartz, calcite, and aggregates in the ith mode, and $K^*_{\text{ext,qzt,i}}$, $K^*_{\text{ext,cal,i}}$, and $K^*_{\text{ext,agg,i}}$ are the normalized extinction coefficients calculated for quartz, calcite, and aggregates in the ith mode. Then the single-scattering albedo ω_0 is calculated as

$$\omega_0 = \frac{K^*_{\text{sc}}}{K^*_{\text{ext}}}. \quad (11)$$

3. Results of Physicochemical Characterization of Dust Aerosols

3.1. Particle Size Distribution

[26] Figure 1 shows mass particle size distributions (MSD) measured for five dust samples: two for Ni-WT, two for Ch-WT and one for Tu-WT. On the basis of these measurements, we consider the size distribution consisting of two modes (hereinafter called fine and coarse modes). Impactor stages 10 and 13 were selected to represent the composition of these modes. Observed similarities in size distributions in terms of position of size modes and their relative proportions are likely due to the generation procedure (i.e., aerosol samples were generated under the same erosion condition simulated in the wind tunnel). To delineate the effect of iron oxides characteristics on dust optics, we use the same size distribution for all samples. Assuming that each mode can be represented by a lognormal function, a median diameter d_{0m} and a dispersion σ determined for the fine mode were $d_{0m} = 3.4$ and $\sigma = 2.0$, and $d_{0m} = 12.4$ and $\sigma = 2.15$ for the coarse mode. The mass fractions of the fine and coarse modes were 26% and 74%, respectively. This MSD was converted to the number size distribution (NSD), which was used in optical calculations. The NSD median diameters for the fine mode and coarse modes were $d_{0n} = 0.8$ μm and $d_{0n} = 2.1$ μm, respectively. The particle number fraction was 94% for fine and 6% for coarse modes.

[27] Our size distribution is consistent with some literature results on dust MSD measured with an impactor. For instance, *Zhang et al.* [2003] found a major particle population for the >16 μm diameter impactor stage and another one between 3 and 6 μm. Mass fractions are also comparable to our values: they report 30/70% for fine/coarse modes. Thus the size distributions measured with the wind tunnel system are consistent with those measured for atmospheric dust aerosols. However, it is important to point out that measurements of dust particle size distributions as well as the lognormal fitting procedure have a number of inherent critical issues [e.g., *Reid et al.*, 2003], especially when measurements are done by means of different techniques. This is the subject of our ongoing research, but it is out of the scope of this paper. Since the focus here is on the role of iron oxide characteristics, the selection of the above size distribution for optical modeling seems to be appropriate.

3.2. Reconstruction of the Relative Amount of Quartz, Calcite, and Aggregates in Fine and Coarse Modes

[28] On the basis of impactor MSD measurements, the number 10 and number 13 impactor stages were selected to represent the composition of the fine and coarse modes, respectively, which is needed for optical modeling (see equations (5)–(7)). The elemental analysis data were used to reconstruct the composition of the dust external mixtures.

[29] Table 2 shows the Ca/Al and Si/Al elemental ratios measured in the bulk aerosol samples as well as in both fine and coarse modes of the three size-segregated samples. Also shown is the particle number percentage of iron oxide–clay aggregates, quartz, and calcite particles calculated with these elemental ratios. Examining Table 2, one can notice that wind tunnel generated samples and atmospheric dust samples have Si/Al ratios over similar ranges. This further confirms that the wind tunnel system is capable of producing dust aerosols with physicochemical properties similar to those of dust observed in real atmospheric conditions.

[30] The values of Si/Al ratios are mainly controlled by the relative proportion of quartz and clay and, thus, by the proportion of coarse and fine mode particles. Indeed, we found that this ratio differs between the two impactor stages selected to represent fine and coarse modes: the coarse mode contains much more quartz than the fine one. This is in agreement with previous studies of atmospheric dust [*Alfaro et al.*, 1998]. Furthermore, the Si/Al ratio varies little for bulk filters regardless of the aerosol type (less than 30% of the mean value) but this ratio significantly differs between samples from different regions. Comparing source bulk aerosols, generated under the same erosion condition, one can see significant differences, at the 5% confidence

Table 2. Elemental Ratios of Ca/Al and Si/Al and Reconstructed Mineralogical Composition (Shown As Percentage Number of Iron Oxide–Clay Aggregate, Quartz, and Calcite) for All Bulk Samples and for Fine and Coarse Modes[a]

Aerosol Sample	Ca/Al (SD)	Si/Al (SD)	Percent N_{agg} (SD)	Percent N_{qzt} (SD)	Percent N_{cal} (SD)
Bulk Samples					
Tu-WT	2.37 (0.06)	2.89 (0.01)	47 (1)	15 (0.1)	38 (1)
Ni-WT	0.06 (0.02)	2.67 (0.07)	78 (2)	20 (1)	2 (1)
Ch-WT	1.38 (0.08)	2.93 (0.05)	56 (1)	18 (0.4)	26 (1)
Ni-Ha	0.33 (0.18)	2.89 (0.61)	71 (11)	21 (9)	7 (3)
Ni-LE	0.04 (0.03)	2.23 (0.16)	88 (4)	11 (4)	1 (1)
Ch-ZBT	0.69 (0.02)	2.77 (0.01)	66 (0.4)	19 (0.4)	16 (0.4)
CV-Sl	0.12 (0.02)	2.33 (0.12)	84 (3)	13 (3)	3 (1)
CV-CS	0.09 (0.02)	2.15 (0.05)	89 (1)	9 (1)	3 (1)
CV-SM	0.16 (0.004)	2.52 (0.04)	79 (1)	17 (1)	4 (0.1)
Size-Resolved Samples					
Tu-WT fine mode	2.07	2.58	52	12	37
Tu-WT coarse mode	3.34	3.47	38	19	43
Ni-WT fine mode	0.04 (0.01)	2.14 (0.12)	90 (3)	9 (3)	1 (0.4)
Ni-WT coarse mode	0.09 (0.02)	4.71 (0.17)	53 (1)	46 (2)	2 (0.4)
Ch-WT fine mode	1.23 (0.06)	2.70 (0.02)	59 (1)	16 (0.1)	25 (1)
Ch-WT coarse mode	1.96 (0.04)	3.93 (0.38)	43 (2)	27 (4)	29 (2)

[a]Values are averaged for all analyzed filters for a given type of sample. The numbers in parentheses are the standard deviations.

level, between the Ni-WT sample and Ch-WT and Tu-WT samples. The former has the Si/Al ratio of 2.63, whereas the latter two have 2.93. In this case the difference is only due to the nature of parent soils.

[31] Note that in addition to the relative proportion of clays and quartz, the nature of aluminosilicates species (especially clays) also can control the Si/Al value. The aluminosilicates species are known to differ in soils of different geographical regions. Because the two effects, i.e., size-dependent aging processes and the nature of parent soils, can affect Si/Al values of atmospheric dust samples, it is not surprising to observe a larger variability in Si/Al in atmospheric samples (2.1–2.9) compared to the wind tunnel generated samples (2.7–2.9). The Si/Al values reported in the literature for the atmospheric dust vary in the range from 2 to 4 [e.g., *Gomes and Gillette*, 1993; *Chiapello et al.*, 1997; *Zhang et al.*, 2003]. Thus our values are consistent with those reported in the literature and represent quite well the natural variability in dust mineralogy.

[32] One also can notice the large variability of Ca among the dust samples. Our measurements show that Chinese and Tunisian samples are rich in calcium, whereas Niger samples are not. This variability in Ca reflects the differences in dust sources. The variability of Ca has been also pointed out in the literature, at least in terms of the Ca/Al ratio which can range from less than 0.2 to as high as 3.8 [e.g., *Chiapello et al.*, 1997; *Formenti et al.*, 2001; *Zhang et al.*, 2003]. This is also supported by X-ray diffraction measurements that have been performed on the wind tunnel samples. These measurements clearly showed that our Tu-WT sample has the highest calcite content, while Ch-WT contains some calcite and Ni-WT has no calcium carbonate [*Lafon*, 2004]. However, the above range of calcite amount is not only due to different sources but also reflects the lost of calcite caused by aging processes in the atmosphere. All long-range transported samples considered here show the lowest values of Ca/Al (see Table 2). In terms of optical properties, the presence of calcium carbonates may lead to lower absorption of the mineral mixture because these species do not absorb light in the solar spectrum.

3.3. Bulk Iron Content of Dust Aerosols

3.3.1. Total Iron Content

[33] Table 3 presents the total iron content measured in aerosol bulk samples in terms of the Fe_2O_3 mass percentage of the total oxide mass and as the Fe/Al elemental ratio. Shown are mean values (averaged for all filters of each aerosol types) and standard deviation (numbers in brackets). The volume fraction ν of iron oxides (calculated with equation (8)) is also shown.

[34] The total iron content (the Fe_2O_3 percentage) varies from 6.2% to 8.7%. The results for atmospheric samples and wind tunnel generated samples show good consistency. The three wind tunnel samples seem to reflect well the variability of our atmospheric samples. The regional and seasonal variability of iron concentrations in the atmosphere over oceans was pointed out, for example, by *Gao et al.* [2001]. In order to delineate the natural variability of iron in dust aerosols around the world, we compared our results

Table 3. Measured Total Iron Content in Aerosol Bulk Samples Presented As the Fe_2O_3 Mass Percentage of the Total Oxide Mass and as the Fe/Al Elemental Ratio[a]

Aerosol Sample	Percent Total Fe_2O_3 (SD)	Total Fe/Al (SD)	ν Calculated From Total Iron			
			HK	GK	HI	GI
Tu-WT	6.2 (0.1)	0.57 (0.02)	0.079	0.105	0.055	0.073
Ni-WT	8.7 (0.2)	0.55 (0.03)	0.076	0.100	0.052	0.070
Ch-WT	7.0 (0.2)	0.60 (0.03)	0.082	0.109	0.057	0.076
Ni-Ha	6.3 (0.9)	0.43 (0.03)	0.061	0.081	0.042	0.056
Ni-LE	7.8 (0.4)	0.42 (0.03)	0.059	0.079	0.041	0.055
Ch-ZBT	7.7 (0.3)	0.60 (0.02)	0.082	0.108	0.057	0.076
CV-Sl	7.6 (0.1)	0.44 (0.02)	0.062	0.082	0.043	0.057
CV-CS	8.2 (0.2)	0.45 (0.01)	0.064	0.085	0.044	0.059
CV-SM	8.5 (0.2)	0.53 (0.01)	0.074	0.098	0.051	0.068

[a]Shown are mean values (averaged for all filters of each aerosol type) and standard deviations (numbers in parentheses). Volume fractions ν of iron oxides calculated for hematite-kaolinite (HK), goethite-kaolinite (GK), hematite-illite (HI), and goethite-illite (GI) aggregates are also shown.

Table 4. Free Iron Contents Measured in Bulk Dust Aerosol Samples Presented As Fe_2O_3 Mass Percentage of the Total Oxide Mass and As Free Fe/Al and Structural Fe/Al Ratios[a]

Aerosol Samples	Percent Free-Fe_2O_3 (SD)	Free-Fe/Al (SD)	Struc-Fe/Al (SD)	Percent Free/Total-Fe (SD)	ν Calculated From Free Iron			
					HK	GK	HI	GI
Tu-WT	3.6 (0.2)	0.33 (0.02)	0.24 (0.01)	58.1 (3.0)	0.048	0.064	0.033	0.044
Ni-WT	6.5 (0.1)	0.41 (0.02)	0.13 (0.01)	75.4 (1.0)	0.058	0.077	0.040	0.054
Ch-WT	3.0 (0.2)	0.26 (0.02)	0.34 (0.01)	43.2 (1.2)	0.037	0.050	0.026	0.034
Ni-Ha	2.8 (0.8)	0.19 (0.05)	0.25 (0.05)	43.3 (10.3)	0.027	0.037	0.019	0.025
Ni-LE	5.0 (0.4)	0.27 (0.02)	0.15 (0.03)	64.7 (4.5)	0.039	0.053	0.027	0.036
Ch-ZBT	3.6 (0.4)	0.28 (0.03)	0.32 (0.02)	46.5 (3.3)	0.040	0.054	0.027	0.037
CV-Sl	4.2 (0.2)	0.24 (0.02)	0.20 (0.01)	54.9 (2.8)	0.035	0.047	0.024	0.032
CV-CS	4.5 (0.4)	0.25 (0.02)	0.20 (0.02)	55.0 (4.3)	0.036	0.049	0.025	0.033
CV-SM	4.7 (0.3)	0.30 (0.02)	0.24 (0.02)	55.0 (3.0)	0.043	0.057	0.029	0.039

[a]Ratios of free to total iron are also given. Shown values are averages for all filters for a given aerosol type. Numbers in parentheses are standard deviations. Volume fractions ν calculated for HK, GK, HI, and GI aggregates using free-Fe/Al are also shown.

against the data reported in the literature. Because elemental analysis is often presented for only a few elements, for comparison purposes we computed the iron content percentage of the sum of Al_2O_3, SiO_2, CaO, and Fe_2O_3 masses only. In this way, our values for the iron content vary from 6.8 to 9.2%. Note that the way in which the iron percentage is calculated could result in nonnegligible differences. Percentage values of the iron content calculated in the same way from several data sets reported by previous studies vary mainly between 4 and 11% [e.g., *Gomes and Gillette*, 1993; *Chiapello et al.*, 1997; *Zhang et al.*, 2003]. Our values are within this range but they are different enough to capture some of the natural variability among different sources. Thus with respect to the total iron content, wind tunnel samples are consistent with atmospheric dust data.

[35] The total iron oxide percentage is not the best way to characterize the iron amount in the samples because this quantity is affected by mass of elements associated with minerals not containing iron (e.g., Si in quartz and Ca in calcite). Another way to characterize the iron content is to look at Fe/Al ratios. In our study the Fe/Al ratio was found to be in the range from 0.4 to 0.6 (see Table 3). The values agree well with the 0.4–0.7 range reported in the literature [e.g., *Gomes and Gillette*, 1993; *Chiapello et al.*, 1997; *Formenti et al.*, 2001]. The considered set of samples does not reveal any clear variation in the total iron content depending on the distance from the source since both the lower value (0.42 for Ni-LE samples) and the higher value (0.60 for Ch-WT samples) were found for source dust aerosols. With regard to the effect of the source region on dust aerosols, the two Chinese samples seem to have higher Fe/Al values than the African ones. But because of a limited number of samples considered here, these results would need to be further verified for a large number of Asian samples. Anyway, it appears that the variability of the total iron content in bulk dust aerosol samples is too complex to be explained by only one factor alone (either aging during the transport or origin).

3.3.2. Free Iron Content

[36] Table 4 presents the results of the free iron content measured for all bulk samples in several different ways: as the Fe_2O_3 percentage of the total oxide mass (see section 2.2.1), as the Fe/Al elemental ratio, and as the free-to-total iron ratio. The aggregate composition (in terms of the volume fraction ν), calculated using the free-Fe-to-Al ratios, are also given in Table 4.

[37] The free iron content is around half that of total iron. Thus this optically active part comprises only a small fraction of the total aerosol mass. Because there are similar amounts of structural and free iron, the amount of total is not representative of the amount of free iron. Furthermore, the variability of the free iron content (2.8–6.5%) is larger than that of total iron (6.2–8.7%). Indeed, the relative standard deviation for the free iron content is 27% versus 12% for total iron. This suggests that the spatiotemporal variability of absorbing properties of dust aerosols due to iron oxides could be more important than that suggested by the total iron content alone. Moreover, the relative mass proportions of the two iron types (free and structural) vary from one aerosol type to another. We found that dust aerosols originating from Niger soils have the largest free iron fraction of total iron (65–75%), while Ch-WT and Ni-Ha samples have the lowest fraction of 43%. The free iron-to-aluminum ratio (free-Fe/Al) was found in the range from 0.19 to 0.41. These values, as well as the percentage content, are more variable for free iron (standard deviation of 12%) than for total iron (standard deviation of 7%).

[38] Analyzing the results, it appears that there is no straightforward relation between free-Fe/Al ratios and the source of dust origin. The free-Fe/Al ratios of 0.26–0.28 found for Chinese samples are not particularly different from African ones (0.19–0.41). Similarly, we could not identify the connection between free-Fe/Al values and the distance from the source. The large differences in free-Fe/Al values obtained for Banizoumbou, Niger, aerosols collected in the atmosphere and those generated in the wind tunnel indicate that the origin is only one of the controlling factors. In this case, it is likely that different erosion conditions contribute to observed differences. Thus free-Fe/Al ratios in aerosols are controlled by both the type of parent soils and erosion processes that affect disaggregation and size fractionation of soil grains.

[39] Note that the interpretation of total iron variability is complicated by the fact that structural iron and free iron exhibit different behaviors. In the case of structural iron, we found some regional specificity: both Chinese samples have similar ratios of structural iron to aluminum (struc-Fe/Al), showing higher values relative to other samples (0.32–0.34). Similarly, both samples from Banizoumbou, Niger, have close struc-Fe/Al values (0.13–0.15). The struc-Fe/Al ratio is controlled by the nature of aluminosilicates and the way iron is involved in their crystal lattice. Previous studies used

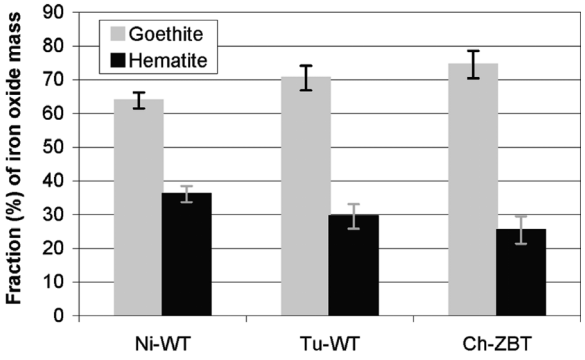

Figure 2. Diffuse reflectance spectroscopy (DRS) measurements made on the Niger wind tunnel sample, on the Tunisia wind tunnel sample, and on the China-Zhenbeitai sample as a fraction of hematite and goethite masses relative to the total mass of iron. Error bars are the standard deviations calculated from four measurements made on each filter.

the mass ratio of clay species as a source tracer, assuming that the mineralogical composition of the aerosol clay fraction is not modified during transport [*Caquineau et al.*, 1998]. If this is the case, then struc-Fe/Al ratios can be expected to remain unchanged during transport. Thus struc-Fe/Al values should be strongly affected by the source region, whereas free-Fe/Al seems to be affected by both the source and emission or transport processes as discussed about.

[40] Nevertheless, observed variability of the iron content is low. The question then arises as to how this variability can affect the optical properties of dust. This issue is addressed in detail in section 4.

3.4. Mineralogy of Iron Oxides

[41] By using the second derivative of the DRS signal (see section 2.2.3.), the relative proportion of hematite and goethite were determined in wind tunnel samples generated from Niger (Ni-WT) and Tunisian (Tu-WT) soils as well as in the atmospheric dust samples collected at Zhenbeitai (Ch-ZBT). The results are presented in Figure 2. We found that in all three cases goethite is the more abundant species comprising about 70(±5)% of the total iron oxide mass. Since goethite and hematite have different light absorption spectra in the visible (goethite is known to be yellow and hematite is red), their relative proportion may play an important role in controlling dust radiative properties. The data on hematite and goethite mass proportions along with the content of iron oxides determined with the CBD method enables us to quantify hematite and goethite mass in dust aerosol samples.

3.5. Size-Resolved Iron Content of Dust Aerosols

3.5.1. Total and Free Iron Mass Percentages

[42] Figure 3a shows the iron content expressed in terms of the Fe_2O_3 percentage (relative to all oxide mass) for three samples generated with the wind tunnel. Total bars represent the total iron content, and free iron fractions are shown as dashed bars. Similar, Figure 3b gives the iron to aluminum mass ratio. The data are shown for the two impactor stages with d_{50} of 2.47 μm and 10.24 μm that were chosen to represent fine and coarse modes, respectively.

[43] First, notice that the total iron content varies with particle size, and that there are some noticeable differences between the dust samples. For instance, the iron content of the 10 μm stage of Chinese dust is significantly different from the 2 μm stage. In turn, the Niger dust sample has the same iron content regardless of particle sizes. Thus there is no common tendency for the size dependence of total iron mass percentage, although when differences do occur in dust aerosol samples considered, the iron content is larger in the coarse mode compared to the fine one. Our results are in agreement, for instance, with those presented by *Eltayeb et al.* [2001]. They also reported the higher iron content in coarser particles of "pure" dust samples collected with the cascade impactor. However, examining the literature, one finds that only a few studies describe the size dependence of iron in aerosol particles. Furthermore, impactor measurements of atmospheric dust can be contaminated by pollution, in which iron originating from industrial processes (i.e., fly ash) is often present. Although this may not be important for bulk mass, elemental ratios in the fine mode can be affected. Another way to explore the dependence of the iron content on particle sizes is to use the electron microscopy. However, previous studies demonstrated some difficulties in determining directly the size-resolved mass of iron with electron microscopy [*Falkovich et al.*, 2001].

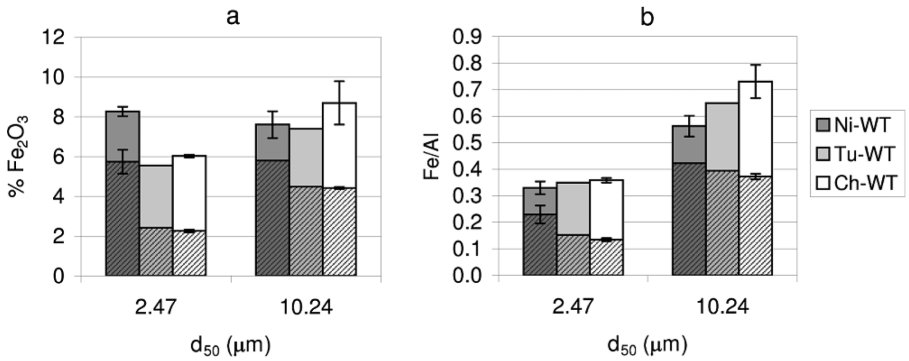

Figure 3. Iron content expressed in terms of (a) Fe_2O_3 percentage (relative to all oxide mass) and (b) iron to aluminum mass ratio for three samples generated with the wind tunnel. Shown are the data for the two impactor stages with d_{50} of 2.24 μm and 10.24 μm that were chosen to represent fine and coarse modes, respectively. Total bars represent total iron, and their dashed parts show the free iron fraction.

Table 5. Total Iron Content of the Fine and Coarse Aerosol Size Modes Presented As Fe_2O_3 Mass Percentage of the Total Oxide Mass and As Fe/Al Ratio[a]

Aerosol Sample	Percent Total-Fe_2O_3 (SD)	Total-Fe/Al (SD)	ν Calculated From Total Iron			
			HK	GK	HI	GI
Tu-WT fine mode	5.5	0.46	0.065	0.086	0.045	0.060
Tu-WT coarse mode	7.4	0.86	0.114	0.149	0.080	0.106
Ni-WT fine mode	8.3 (0.2)	0.44 (0.03)	0.061	0.082	0.042	0.057
Ni-WT coarse mode	7.6 (0.7)	0.78	0.105	0.137	0.073	0.097
Ch-WT fine mode	6.0 (0.1)	0.47 (0.01)	0.066	0.088	0.046	0.061
Ch-WT coarse mode	8.7 (1.1)	0.97 (0.08)	0.127	0.165	0.089	0.117

[a]Values are averages for all filters for a given aerosol type. Numbers in parentheses are standard deviations. Volume fractions ν calculated for HK, GK, HI, and GI aggregates using Fe/Al are also shown.

Also, this technique was not capable of separating free iron from structural iron.

[44] Second, similar to the total iron content, the free iron content of Niger samples remains the same in different size classes. In contrast, Chinese and Tunisian samples have higher free iron in the coarse mode than in the fine one. In all size ranges the free iron content in Niger samples is much higher than that in Tunisian and Chinese samples, unlike in the case of total iron. Thus comparing free iron in different dust samples reveals more differences among them than when considering total iron alone.

[45] The above discussion indicates that all processes that affect the relative proportion of fine and coarse modes can affect the total and free iron content. Given that optical properties of dust strongly depend on the particle size spectrum, below we examine the extent to which differences between fine and coarse modes affect the spectral light absorption of dust mixtures.

3.5.2. Ratios of Total and Free Iron to Aluminum

[46] Referring back to Figure 3b, one can notice various differences between total-Fe/Al and free-Fe/Al ratios. Both ratios show some dependence on size in all three samples: values decrease with decreasing size.

[47] For total iron ratios, three types of aerosols show significant differences for coarse particles but not for fine ones. Coarse particles of the Ch-WT sample have the highest total-Fe/Al value, whereas the Ni-WT sample has the lowest one. But the results for free iron are different: the Ni-WT sample has higher values than Ch-WT and Tu-WT in all sizes, and values remain different even in the fine particles. These differences in free-Fe/Al ratios indicate that both sources and transport potentially affect dust optical properties. Considering only total iron would suggest that, for long-range transported dust aerosols with coarser particles removed, the Fe/Al ratio may be quite homogeneous regardless of the sample. But this will not be the case if one takes into account only free iron. Nonetheless, the natural variability of finest particles may be less important than that of bulk samples, and thus values could be more similar after transport in the atmosphere. This is supported by the long-range transported samples (Table 4). There are only a few studies that addressed the evolution of mineral iron in dust during (dry) transport. For example, *Mori et al.* [2003] reported Fe/Al ratios varying from 0.5 to 0.6 for Asian dust measured along the transport route. These values are in good agreement with our results. However, their samples could be contaminated with urban aerosols.

[48] Tables 5 and 6 summarize the values of the total and free iron contents, respectively, for the two impactor stages considered as representative of fine and coarse size modes. Also given are the volume fraction ν that will be used in optics calculations in section 4.

3.6. Relationships Between the Iron Content of Soils and Aerosol Samples

[49] We suggested previously that both transport processes and origin of dust aerosols can control their iron content. To further address the origin aspect, we compared the iron content in the soils and in dust aerosols generated in the wind tunnel from these soils. In this fashion we exclude the effect of transport processes.

[50] First, we examine the variability of the total iron content in bulk soil samples and compared it to that of bulk aerosol samples. The Fe_2O_3 percentage values (and standard deviation) are 1.6(0.04), 0.5(0.1), and 2.9(0.2) for Tunisian, Niger, and Chinese soils, respectively, and corresponding Fe/Al ratios for these soils are 0.43(0.02), 0.53(0.01), and 0.36(0.02). In terms of the mass percentage, the soil values are very low compared to the bulk aerosols values. This is

Table 6. Free Iron Contents Measured in Fine and Coarse Modes of the Three Wind Tunnel Dust Aerosol Samples Presented As Fe_2O_3 Mass Percentage of the Total Oxide Mass and As Free Fe/Al and Structural Fe/Al Ratios[a]

Aerosol Sample	Percent Free-Fe_2O_3 (SD)	Free-Fe/Al (SD)	Struc-Fe/Al (SD)	Percent Free/Total-Fe (SD)	ν Calculated From Free Iron			
					HK	GK	HI	GI
Tu-WT fine mode	2.4	0.20	0.26	43.7	0.029	0.040	0.020	0.027
Tu-WT coarse mode	4.5	0.52	0.34	60.7	0.073	0.096	0.050	0.067
Ni-WT fine mode	5.7 (0.6)	0.30 (0.04)	0.13 (0.03)	69.4 (5.2)	0.044	0.058	0.030	0.040
Ni-WT coarse mode	5.8	0.56	0.22	71.8	0.078	0.103	0.054	0.071
Ch-WT fine mode	4.4 (0.1)	0.18 (0.01)	0.30 (0.01)	37.6 (0.7)	0.026	0.035	0.018	0.024
Ch-WT coarse mode	2.3 (0.1)	0.49 (0.01)	0.47 (0.01)	51.2 (5.8)	0.069	0.091	0.047	0.063

[a]Ratios of free to total iron in fine and coarse modes are also given. Values are averages of all filters for a given aerosol type. Numbers in parentheses are standard deviations. Volume fractions ν calculated for HK, GK, HI, and GI aggregates using Fe/Al ratios are also shown.

Table 7. Summary of Volume Fractions ν of Iron Oxides in Illite- or Kaolinite-Containing Aggregates Calculated From Free and Total Iron Data Measured for Bulk and Size-Segregated Samples

	ν							
	HI		GI		HK		GK	
Fe/Al Values From	Fine	Coarse	Fine	Coarse	Fine	Coarse	Fine	Coarse
Total iron measured on bulk filters								
Maximum	0.057	0.057	0.076	0.076	0.082	0.082	0.109	0.109
Mean	0.049	0.049	0.066	0.066	0.071	0.071	0.094	0.094
Minimim	0.041	0.041	0.055	0.055	0.059	0.059	0.079	0.079
Free iron measured on bulk filters								
Maximum	0.040	0.040	0.054	0.054	0.058	0.058	0.077	0.077
Mean	0.028	0.028	0.037	0.037	0.040	0.040	0.054	0.054
Minimum	0.019	0.019	0.025	0.025	0.027	0.027	0.037	0.037
Total iron measured with an impactor								
Maximum	0.046	0.089	0.061	0.117	0.066	0.127	0.088	0.165
Mean	0.044	0.081	0.059	0.107	0.064	0.115	0.085	0.150
Minimum	0.042	0.073	0.057	0.097	0.061	0.105	0.082	0.137
Free iron measured with an impactor								
Maximum	0.030	0.054	0.040	0.071	0.044	0.078	0.058	0.103
Mean	0.023	0.050	0.030	0.067	0.033	0.073	0.044	0.097
Minimum	0.018	0.047	0.024	0.063	0.026	0.069	0.035	0.091

because of the mineralogical fractionation occurring during the saltation and sandblasting process discussed above. The Fe/Al ratios are also lower in soils than in aerosols. Moreover, comparing bulk soils and bulk aerosols, one cannot find any clear tendencies. For instance, the Chinese soil sample contains the highest iron content while Chinese dust aerosols do not have the highest values. This indicates that it is problematic to directly relate the total iron content in bulk soils with the total iron content in dust aerosols.

[51] The free iron content of the bulk soils are found to be 0.28, 0.33 and 0.35 g/100g (of soil gravimetric mass) for Niger, Tunisian and Chinese soils, respectively. Similar to total iron, the free iron content of aerosols (see Table 4) is different from soils. For instance, the free iron content is the lowest in Niger soil samples but it is the highest in Niger aerosol samples. There is, once again, no clear relationship between bulk soil and bulk aerosol free iron content, certainly because of the fractionation effect.

[52] We also explore the possibility of a relationship between the iron content in aerosols and different size fractions of soils. This is motivated by the fact that dust aerosols are generated from soil grains coming from the finest fraction of the soil texture (clays and fine silts). The free iron–to–total iron ratio is found to be 0.41 (0.02) and 0.57 (0.01) for Tunisian soil, 0.77 (0.02) and 0.73 (0.01) for Niger soil, and 0.39 (0.02) and 0.38 (0.02) for Chinese in clay and fine silt fractions, respectively. Comparing the fine mode of the aerosol sample with the clay fraction of its parent soil and the coarse mode of aerosols with the fine silt fraction of its parent soil, similarities in terms of free iron–to–total iron ratio are apparent. Since these ratios are often used in soil science as a good indicator of the weathering degree of soils [*Baize*, 2000] and because they should not be as affected by fractionation (in terms of mass percentage), they seem to provide a good linkage between aerosol particles and parent soils.

3.7. Construction of Iron Oxide–Clay Aggregates for Optical Modeling

[53] The data presented above provide new information that enables us to explore how the iron oxide characteristics affect the optical properties of mineral dust aerosols. To date, the most common approach to compute optical properties of mineral dust aerosols required for modeling their radiative effects is to use the refractive indices determined for several bulk samples. As discussed in the introduction, this approach has a number of serious drawbacks. An alternative approach proposed by *Sokolik and Toon* [1999] avoids these drawbacks by taking into account the mineralogical composition of the dust mixture consisting of individual minerals and aggregates. In particular, *Sokolik and Toon* [1999] demonstrated that the iron oxide–clay aggregates are a key factor in controlling light absorption by the dust mixtures. However, due to a lack of data, their modeling studies relied on a number of critical assumptions regarding the iron oxide mineralogy (only hematite was considered), size-resolved composition (the fraction of hematite was considered size-independent), and the amount of iron oxides (no measurements of free iron were available). The data obtained under this study enable us to address all these issues to provide a better understanding of the nature of light absorption by dust.

[54] In this study the iron oxide–clay aggregates were constructed by considering the aggregation of either hematite or goethite with kaolinite or illite resulting in four types of aggregates: hematite-illite (HI), hematite-kaolinite (HK), goethite-illite (GI), and goethite-kaolinite (GK). For each aggregate type, we considered the maximum, minimum and mean values of the volume fraction ν that were determined from Fe/Al values measured for (1) total iron, (2) free iron, and (3) size-resolved free iron. Calculated values of ν are presented in Table 7. These values were used to compute the spectral effective refractive indices of each type of aggregates employing the Bruggeman approximation and the refractive indices of individual end-members. Then the optical characteristics of aggregates were calculated and weighted with those of other species forming the external mixture to give its optical properties (see section 4). Here we model several different mixtures composed of light-absorbing (i.e., iron oxide–clay aggregates) and non-absorbing species (quartz and calcite). We also use the size-resolved data for Ni-WT, Ch-WT, and Tu-WT samples

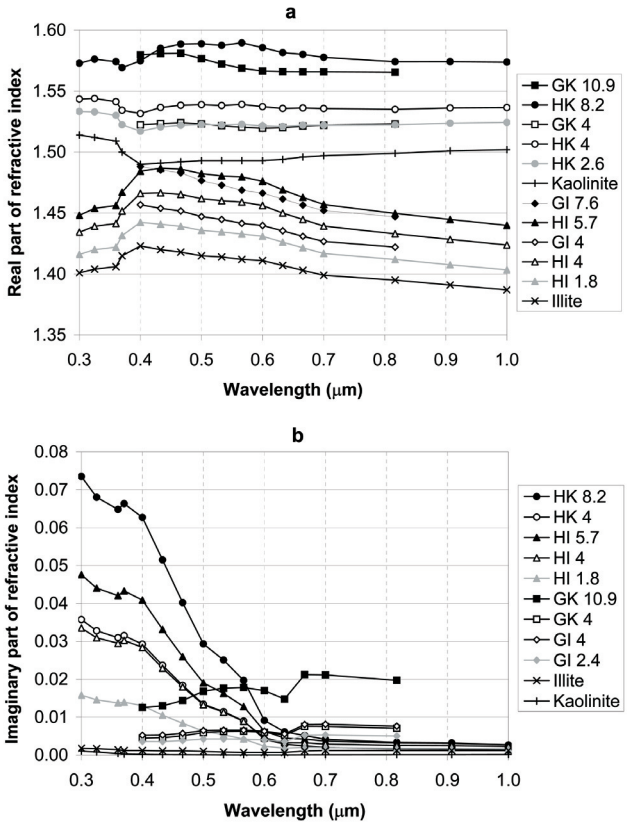

Figure 4. (a) Real and (b) imaginary parts of the refractive index of individual clays (illite and kaolinite) and the effective refractive index of hematite-illite (HI), goethite-illite (GI), hematite-kaolinite (HK), and goethite-kaolinite (GK) aggregates. The numbers in the legend show the volume fraction ν (%) of iron oxide in the aggregate.

to address the regional differences in optical properties. In addition to quartz which is a common mineral in atmospheric dust, we choose to include calcite to account for the large variations of its content determined in the samples. The Tunisian sample (Tu-WT) generated in the wind tunnel has the largest content of calcium carbonate, while Ni-WT is very poor one, and Ch-WT still has high calcite amount, but less than Tu-WT one. For each of these external mixtures, the composition of the aggregates is taken to vary in the range shown in Table 7.

4. Results of Optical Modeling

[55] We start by analyzing the effective refractive indices computed for iron oxide–clay aggregates. Then, we examine the effects of the iron parameters on the wavelength-dependent normalized extinction coefficient, K^*_{ext}, and single-scattering albedo, ω_0, calculated for these aggregates. Finally, the optical properties of the dust mixtures are presented and discussed.

4.1. Optical Properties of Iron Oxide–Clay Aggregates

4.1.1. Effective Refractive Indices

[56] Calculations were done for all cases presented in Table 7. Figure 4 shows some examples to illustrate several important features in the behavior of effective refractive indices of iron oxide–clay aggregates that will be helpful for interpreting their optical properties.

[57] First, note that the volume fraction ν of iron oxide in an aggregate depends on both clay and iron oxide mineralogical speciation. Indeed, for the same range of Fe/Al (from 0.18 to 0.60), ν values vary from 0.026 to 0.082 for hematite-kaolinite aggregates, from 0.035 to 0.109 for goethite-kaolinite aggregates, from 0.018 to 0.057 for hematite-illite aggregates, and from 0.024 to 0.076 for goethite-illite aggregates. Note that for the same elemental iron amount, one always finds a higher volume fraction of iron oxides if goethite and kaolinite are selected to represent iron oxides and clays in the aggregate.

[58] Figure 4a shows the minimum and maximum values obtained for the real part of the effective refractive indices of both illite- and kaolinite-containing aggregates, as well as the real part of refractive indices of pure illite and pure kaolinite. We also show the values obtained for each type of aggregates with the same iron oxide amount ($\nu = 0.04$).

[59] The real part of the refractive index of illite-containing aggregates ranges between 1.4 and 1.5, while kaolinite-containing aggregates show somewhat higher values between 1.5 and 1.6 in the visible spectrum. For the range of iron oxide amounts considered, illite-containing aggregates always have smaller real parts compared to kaolinite-containing ones. An increase in the iron oxide fraction results in the increasing real part. Adding the same amount (for instance, $\nu = 0.04$) of hematite or goethite to either illite or kaolinite causes an increase of the real part of iron oxide–clay aggregates, though hematite causes a slightly higher increase than goethite. Note that the maximum values of the real part of effective refractive indices of hematite-containing aggregates are higher than those of goethite-containing aggregates, even though the volume fraction of iron oxide is smaller in the latter case. We conclude that the real part of effective refractive indices is more sensitive to clay mineralogy and amount of iron oxides in the aggregates than to the iron mineralogy.

[60] In turn, the imaginary part of the effective refractive index is affected little by the type of clay. Comparing hematite-illite and hematite-kaolinite aggregates with the same content of iron oxides (e.g., $\nu = 0.04$), we observe very similar values (Figure 4b). However, one needs to keep in mind that the clay species plays an important role in calculations of the volume fraction of iron oxide in the aggregates. For instance, for the same Fe/Al value (e.g., 0.60) and for a given iron oxide, the composition of aggregates varies from $\nu = 0.057$ for hematite-illite aggregates to $\nu = 0.082$ for hematite-kaolinite aggregates, resulting in noticeable differences in the effective refractive indices (Figure 4b). Thus with respect to the imaginary part of the effective refractive index and hence light absorption by aggregates, the type of clays is important in determining the fraction of iron oxides, while the imaginary part of clay refractive indices itself plays little role. Compared to pure clay species, the imaginary part of the aggregates is always much higher.

[61] Changing the amount of iron oxides involved in aggregates strongly affects their effective refractive index. For example, hematite-kaolinite aggregates with a low iron content ($\nu = 0.026$) have an imaginary part of 0.009 at

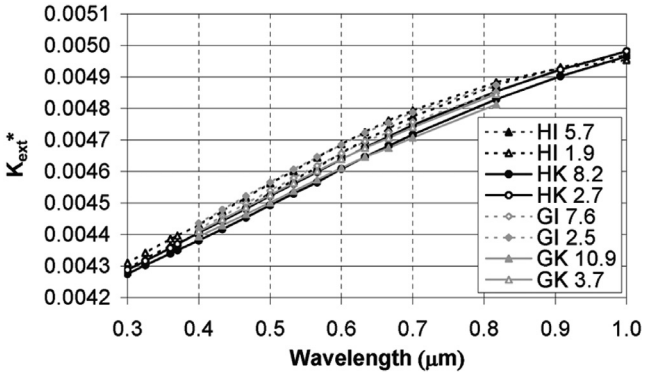

Figure 5. Normalized extinction coefficients as a function of wavelength computed for HI, GI, HK, and GK aggregates using the maximum and minimum ν values measured in bulk samples. The numbers in the legend give the volume fraction ν (%) of iron oxide in the aggregate.

0.5 μm, while aggregates with a high iron content (ν = 0.082) have an imaginary part of 0.029 at the same wavelength. Unlike the real part, the imaginary part of effective refractive indices differs between hematite- and goethite-containing aggregates. These differences are in both the different spectral dependence of the imaginary refractive indices as well as their values. Toward the shorter wavelengths, hematite-containing aggregates show larger values of the imaginary part than goethite-containing ones, while at the longer wavelengths the latter aggregates have the higher values but not as high as hematite-containing aggregates at the shorter wavelengths.

4.1.2. Extinction Coefficient

[62] Figure 5 shows the normalized extinction coefficients K_{ext}^* calculated for iron oxide–clay aggregates considering the free and total iron content. For a given type of clay, the normalized extinction coefficient varies little with the iron parameters. Therefore we conclude that the extinction coefficient is not very sensitive either to the mineralogy of iron oxides or to their amount in aggregates (in the range considered). On the other hand, one can notice some differences between illite- and kaolinite-containing aggregates: the extinction coefficient of the former is always higher than that of the latter. Because the main difference between kaolinite and illite lies in the real part of their refractive indices and because the imaginary part of the effective refractive index of aggregates is mainly controlled by the iron oxide content, one can conclude that the extinction coefficient (and hence the aerosol optical depth) is more sensitive to the real part than to the imaginary one. Nevertheless, some differences between K_{ext}^* of illite- and kaolinite-containing aggregates can be observed that could become important in the case of a heavy dust load in the atmosphere. Examining the changes in the normalized extinction coefficient, we found that relative changes ($\Delta K_{ext}^*/K_{ext}^*$) do not exceed 0.6% regardless of the wavelength. Moreover, this holds if one considers each size mode independently, though the coarse mode has larger K_{ext}^* compared to the fine one. Thus our results show that the mineralogical composition of aggregates has negligible effect on the extinction coefficient and optical depth in the visible spectral range.

4.1.3. Single-Scattering Albedo

[63] Unlike the extinction coefficient, the single-scattering albedo of the aggregates is strongly affected by the iron oxide parameters. In particular, ω_0 calculated from the total iron content shows significant differences compared to one calculated from the free iron content as shown in Figure 6. It is apparent that the distinction between free iron and total iron is required to make predictions of ω_0 and hence the dust radiative effects of mineral dust more realistic. We also would like to point out that the retrieval of ω_0 from the optical depth (extinction coefficient) measurements is unlikely to give satisfactory results because of very different sensitivities of K_{ext}^* and ω_0 to iron oxides parameters.

[64] Figure 7 shows ω_0 calculated for the fine and coarse modes using free-Fe/Al and total-Fe/Al data. The differ-

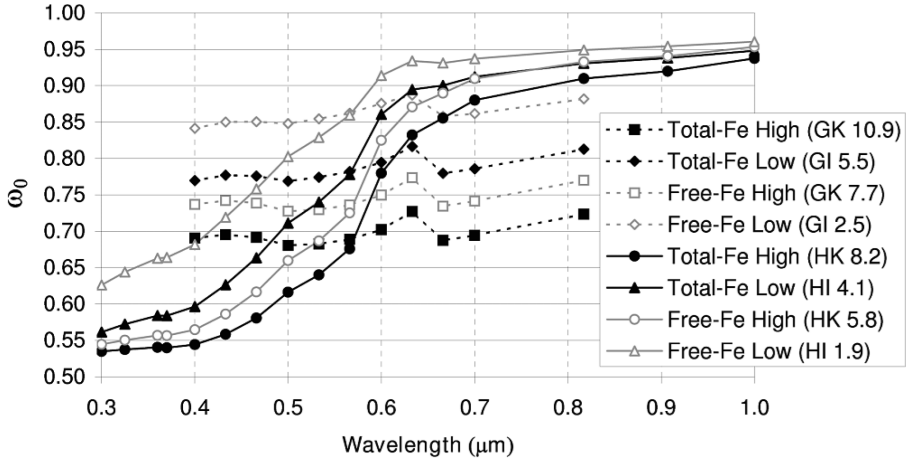

Figure 6. Single-scattering albedos as a function of wavelength calculated for HI, GI, HK, and GK aggregates using the volume ν fraction of iron oxides (shown in percentage in brackets) determined from the measured total iron content or free iron content. Calculations were made for the lowest and highest values of ν determined in all samples considering hematite-containing and goethite-containing aggregates and in the case of free and total iron.

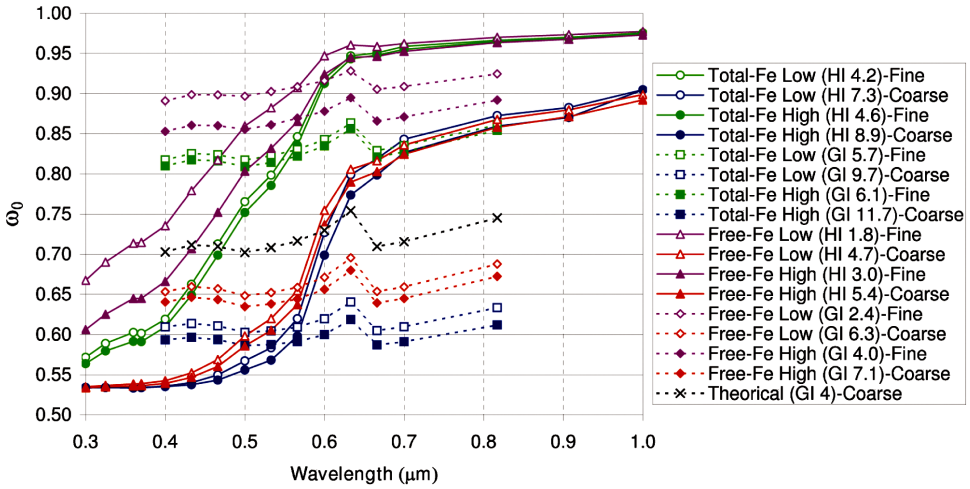

Figure 7. Single-scattering albedos as a function of wavelength calculated for fine and coarse modes of GI or HI aggregates. Calculations were done with a low and a high iron content (shown as the volume fraction ν in percentage) and for total and free iron-to-aluminum ratios measured on impactor stages 10 and 13 for Ni-WT and Ch-WT samples. The black curve is for the goethite-illite aggregate with the 4% volume fraction of goethite.

ences in ω_0 observed for bulk samples (Figure 6) in the case of total and free iron are similar to those in the case of fine and coarse size modes. Notice that coarse-size aggregates have much lower single-scattering albedo compared to fine aggregates. This is due to both size and the fact that coarse aggregates contain more iron oxides than fine ones. Indeed, even assuming that fine and coarse modes have the same iron oxide amount (e.g., $\nu = 0.04$ (Figure 7)), ω_0 of coarse aggregates are lower compared to fine ones.

[65] Figure 8 compares ω_0 computed with size-resolved free iron content against those calculated by using free-Fe/Al values of bulk samples. Results obtained with size-resolved free-Fe are not so much different from those of the bulk ones. This implies that for a given dust aerosol sample, collected in a particular place at a given time, measurements of size-resolved free iron content add little to improving the optical properties, so the information on bulk free-Fe content seems to be sufficient. However, if one is interested in predicting the evolution of optical properties of dust particles as they are transported in the atmosphere undergoing physical and chemical changes which are size-dependent, size-resolved data on free-Fe would be critical. Given the large differences in ω_0 between fine and coarse modes, one can expect that the single-scattering albedo changes during dust transport, and that dust is likely to be less absorbing downwind from the source because of the preferential removal of coarse particles.

[66] Analyzing Figure 6, one can notice the large range of ω_0 values in both free and total iron cases. For instance, ω_0 ranges from 0.71 to 0.84 at 0.55 μm when calculations are

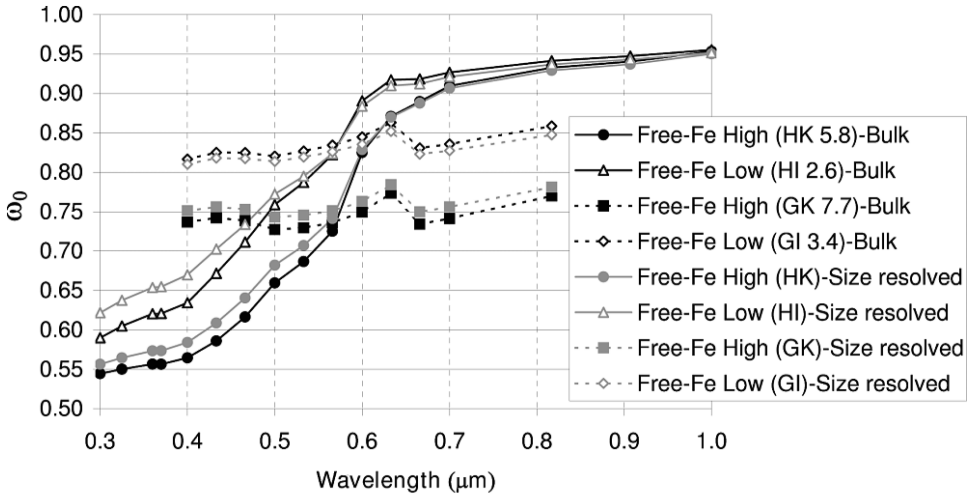

Figure 8. Single-scattering albedos as a function of wavelength calculated for iron oxide–clay aggregates (HK, GK, GI, and HI) using the free iron content of bulk samples or the size-resolved iron content. Cases shown are for the maximum and minimum free iron content for both hematite- and goethite-containing aggregates.

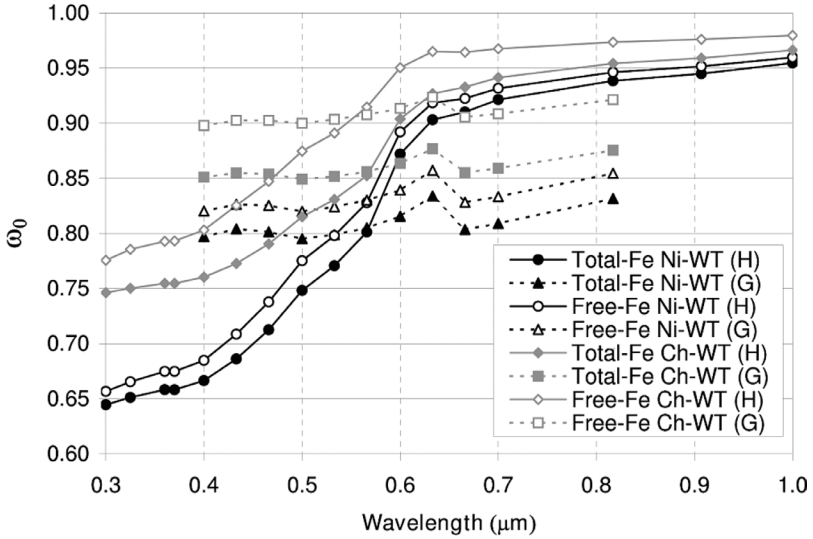

Figure 9. Single-scattering albedos as a function of wavelength computed for the external mixture of quartz, calcite, and HI or GI aggregates, reconstructed from measurements of total iron and free iron for the Ni-WT and Ch-WT samples.

performed with maximum and minimum values of the free iron content measured in aerosol samples (assuming that iron oxide is hematite). Thus in addition to the free status of iron, the natural variability of its amount is an important factor controlling the single-scattering albedo of aggregates. Although the range of free-Fe/Al (0.19–0.41 in our samples) seems to be not so large, this variability apparently causes large differences in ω_0 and thus is of importance to radiation/climate modeling.

[67] The results shown in Figure 6 are obtained from calculations made both for illite- and kaolinite-containing aggregates. By comparing the effective refractive indices of aggregates (section 4.1.1), we already pointed out that the clay mineralogy does not affect the absorbing properties directly (i.e., via the refractive index of clays themselves). However, the choice of a clay species affects the calculated volume fraction of iron oxides in aggregates. Thus for a same iron oxide species, existing differences in ω_0 between illite- and kaolinite-containing aggregates are mainly due to the varying amount of iron.

[68] Another important point to notice is the role of iron oxide mineralogy: goethite versus hematite (see Figure 6). Hematite-containing aggregates show a very low single-scattering albedo at the short wavelengths and a high one at the longer wavelengths. In contrast, ω_0 of goethite-containing aggregates have a low spectral variability. Therefore ω_0 values of goethite-containing aggregates are higher than those of hematite-containing aggregates at the short wavelengths and lower at the longer wavelengths. These differences in ω_0 are similar to those in the imaginary part of the effective refractive index of these two species discussed above. Because of the lack of data on the refractive index of goethite, we are not able to compute ω_0 of goethite-containing aggregates at a wavelength less than 0.45 μm and greater than 0.75 μm. Nevertheless, it seems that existing differences between hematite- and goethite-containing aggregates are large enough to be important in predicting the radiative impacts of dust. Moreover, our measurements show that both species are present in each dust sample and that goethite is more abundant than hematite in mineral aerosols. However, above calculations were performed by assuming either hematite or goethite because data on mass fractions of two iron oxides obtained in our study cannot be used directly to calculate the relative number of hematite-clay aggregates and goethite-clay aggregates. Indeed, such calculations would require information on the association state between hematite and goethite and clay minerals in aggregates. To the best of our knowledge, no prior studies reported this information. Here we address this problem by introducing some assumptions that enable us to model optical properties of an external mixture containing both hematite- and goethite-containing aggregates, as described in the next section.

4.2. Optical Properties of the Mixtures of Iron Oxide–Clay Aggregates and Nonclay Particles

[69] To test the effect of iron oxide parameters on realistic mineral mixtures, we calculated optical properties of an external mixture consisting of iron oxide–clay aggregates and nonclay particles for the three generated dust aerosol samples. Unlike quartz and calcite that do not absorb in the visible, the aggregates exhibit different absorbing properties as a function of iron parameters chosen to calculate their optical properties as discussed above. The composition of the external mixtures as well as aggregates was constrained by data obtained in our measurements (see sections 3.2 and 3.5).

[70] We found that the normalized extinction coefficient computed for the external mixtures of aggregates and nonclay minerals behaves similarly to that of iron oxide–clay aggregates themselves. This could be expected since the real parts of the refractive index of our nonabsorbing species (quartz and calcite) are close to the ones of illite and kaolinite [*Sokolik and Toon*, 1999]. Thus we conclude that the normalized extinction coefficient has little sensitivity to the composition of mineral aerosols, neither to the composition of iron oxide–clay aggregates nor to the composition

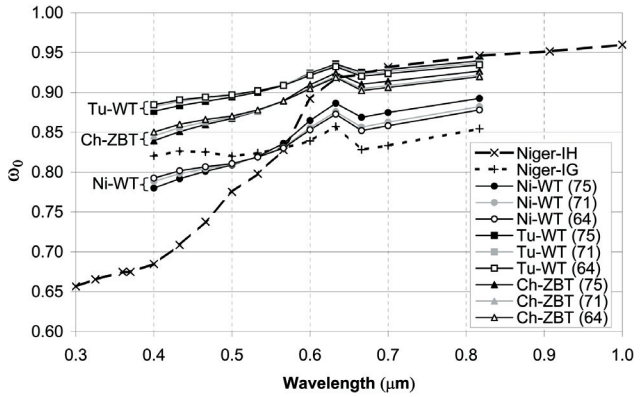

Figure 10. Single-scattering albedos as a function of wavelength computed for the external mixture of quartz, calcite, GI aggregates, and HI aggregates, reconstructed for three aerosol samples: Tu-WT, Ni-WT, and Ch-ZBT. Calculations were done with the three measured values of the goethite mass fraction: 75%, 71%, and 64% (shown in parentheses). To compare, single-scattering albedos computed for Niger considering either hematite or goethite are also shown.

of the external mixture of aggregates and other nonabsorbing species.

[71] Figure 9 shows examples of the single-scattering albedo computed for the external mixtures in which aggregate compositions (considering only illite-containing aggregates) were calculated either with total iron or with free iron data from bulk samples. In these examples, mineralogical compositions were inferred from the elemental composition of the bulk Ni-WT and Ch-WT samples. Here considering free iron content instead of total iron content leads to significantly different values of the single-scattering albedo despite the presence of nonabsorbing species in the mixture. For instance for the Ch-WT sample, calculations made with hematite-illite aggregates give ω_0 from 0.84 to 0.90 at 0.55 μm when the iron amount is calculated from total iron or free iron, and in the range from 0.85 to 0.91 when calculations are made for goethite-illite aggregates. The effect of hematite versus goethite on the spectral behavior of the single-scattering albedo of the mixture is clearly observed in Figure 9.

[72] Natural variability of the free iron content also remains important in the case of the external mixture since the use of high and the low values of free iron content in calculations resulted in very different values of ω_0. Calculations were made with the size-resolved mineralogical composition of Ni-WT, Ch-WT and Tu-WT samples considering the cases of the maximum and minimum free iron content. For both goethite and hematite, we obtained the spectral behavior of ω_0 similar to that showed in Figure 9. At 0.55 μm, the single-scattering albedo for the Niger sample varies from 0.84 to 0.87 depending on the high or low free iron content values, while ω_0 values of the Chinese and Tunisian samples vary from 0.88 to 0.91 and from 0.90 to 0.92, respectively. Thus despite the differences in relative abundance of aggregates and nonabsorbing species in samples considered, variability in the iron oxide content remains an important factor in controlling the single-scattering albedo of mixtures. The differences in ω_0 are clearly seen for the high and low iron contents in each of the three aerosol samples. Although the Chinese sample has lower iron oxide content than the Tunisian sample, ω_0 calculated for these aerosols are very similar. This indicates that in addition to the iron oxide amount, the relative proportion of absorbing aggregates and nonabsorbing minerals is another important factor affecting the single-scattering albedo.

[73] Up to this point, optical calculations were done for two extreme cases in which all iron oxides were considered either as hematite or goethite. However, our measurements showed that both species can be present in the same dust sample. Unfortunately, as we explained previously, we do not have enough data to constrain exactly either the fraction of these species or how this fraction changes with size. Instead, we introduce a number of assumptions that allow us to model the optical properties of mixtures containing both hematite- and goethite-containing aggregates along with nonabsorbing species. It was assumed that aggregates are made of illite and that ν is the same for hematite- and goethite-illite aggregates. The latter assumption is an important simplification that requires further examination. The volume fraction ν was calculated using measured free-Fe/Al ratios of bulk samples and hematite/goethite mass ratios obtained for Ni-WT, Tu-WT, and Ch-ZBT samples. Calculated ω_0 are shown in Figure 10. For each of the Ni-WT, Tu-WT and Ch-WT samples, three cases were considered using 64%, 71%, and 75% goethite mass fractions based on our measurements (see Figure 2). To compare, ω_0 computed for the Niger sample considering iron oxide either as hematite or goethite are also shown. One can notice large differences between these ω_0 and those calculated for the mixtures containing both hematite-clay and goethite-clay aggregates. The latter ω_0 are closer to those calculated with goethite than those with hematite. However, ω_0 show stronger dependence on the wavelength when both HI and GI aggregates are present compared to the GI only case. Observed differences between the nine curves shown in Figure 10 are controlled by three factors: the relative number of light-absorbing aggregates and nonabsorbing species (quartz and calcite), ν, and goethite mass fraction. A closer examination of Figure 10 reveals that the varying goethite mass fraction exerts a relatively small effect. This suggests that, under the assumptions of the homogeneous partitioning of hematite and goethite in iron oxide–clay aggregates (i.e., same ν) and given the low variability of hematite/goethite mass ratios found in our samples, an assumption that goethite represents 70% of the total mass of the iron oxides is a good approximation for optical calculations. In any case, this will need to be confirmed by additional measurements of the goethite/hematite mass ratio in different dust aerosol samples as well as by new studies on the mixing state of the iron oxide–clay aggregates.

[74] Figure 11 presents ω_0 computed for Tu-WT, Ni-WT, and Ch-WT samples using measurements of size-resolved elemental composition and size-resolved free-Fe/Al ratios. The Niger sample is rather poor in nonclay minerals, because it contains little calcite (see Table 2). This implies that the fraction of iron oxide–clay aggregates is much higher in the Niger sample compared to other two. At the

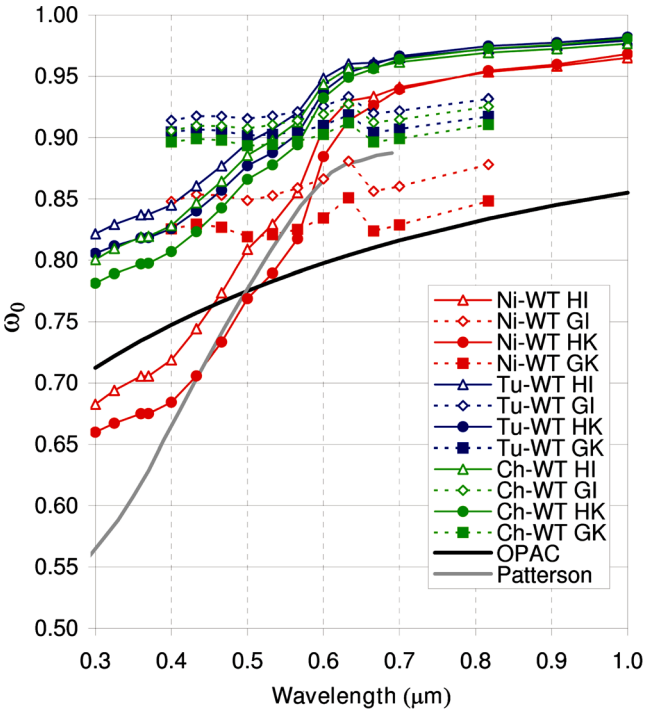

Figure 11. Single-scattering albedos as a function of wavelength computed for external mixtures of nonabsorbing species and iron oxide–clay aggregates (HI, GI, GK, and HK), reconstructed from the elemental composition and free iron content measured on impactor stages for the three samples generated in the wind tunnel: Ni-WT, Tu-WT, and Ch-WT. Single-scattering albedos calculated with the OPAC and *Patterson et al.* [1977] refractive indices are also shown.

same time, the Niger sample is rich in free iron and has the largest number of iron oxide–clay particles. As a result, its single-scattering albedo is much lower in the visible than that of Chinese aerosol. Our Tunisian sample, having the largest number nonabsorbing particles, has the lowest relative number of aggregates. Although the Chinese sample has the lowest free iron content, its ω_0 values are not the highest. Indeed, the Tunisian aerosols have a higher single-scattering albedo because they contain many nonabsorbing particles, though the Chinese sample has less free iron. This indicates that the single-scattering albedo is significantly affected both by the quantities of free iron involved in the aggregates and the relative proportion of these aggregates and nonabsorbing particles. Both factors depend on the dust source and thus have the regional nature.

[75] Finally, Figure 12 presents the likely single-scattering albedo of three dust samples (Ni-WT, Ch-WT, and Tu-WT) computed for the considered size distribution by taking into account all relevant data obtained in this study. In particular, we used the size-resolved information for both the mineralogical composition and the fraction ν of iron oxides in aggregates. Yet a number of assumptions were required. On the basis of our measurements and literature data on the regional abundance of clays (see section 2.3), kaolinite was chosen to represent the clay species in aggregates for the Ni-WT sample, whereas illite was used for both Tu-WT and Ch-WT. Also, it was assumed that goethite comprises 70% the mass of iron oxides in both fine and coarse modes. Although these assumptions affect ω_0 shown in Figure 12 to some extent, the importance of regional variability of iron oxide characteristics and the relative proportion of absorbing aggregates and nonabsorbing minerals is readily apparent. Furthermore, Figure 12 also shows ω_0 computed with commonly used refractive indexes of *Patterson et al.* [1977] and OPAC dust-like [*d'Almeida et al.*, 1991; *Hess et al.*, 1998]. One can notice significant differences in values and spectral behaviors of ω_0 compared in Figure 12. Clearly, neither *Patterson et al.* [1977] nor OPAC dust-like refractive indices are capable of reproducing the regional signature of mineral dust.

5. Conclusions

[76] For the first time several atmospheric dust samples as well as samples generated in a laboratory wind tunnel were analyzed for their total and free iron content, iron oxide mineralogy, and particle size distribution. The new methodology was developed to incorporate this information into optical modeling. Applying the methodology to the unique data set obtained in this study enabled us to investigate the role of iron oxide characteristics in light absorption by dust aerosols. A summary of our findings and implications are as follows.

[77] 1. Measurements demonstrated that the total iron content when expressed as a percentage of total mass varies little between the samples regardless of their origin or aging. However, Fe/Al ratios do vary depending on dust origin. The Chinese dust sample has the highest Fe/Al ratios relative to Niger and Tunisian ones. Analysis of a larger number of regional dust samples will be required to further explore this tendency.

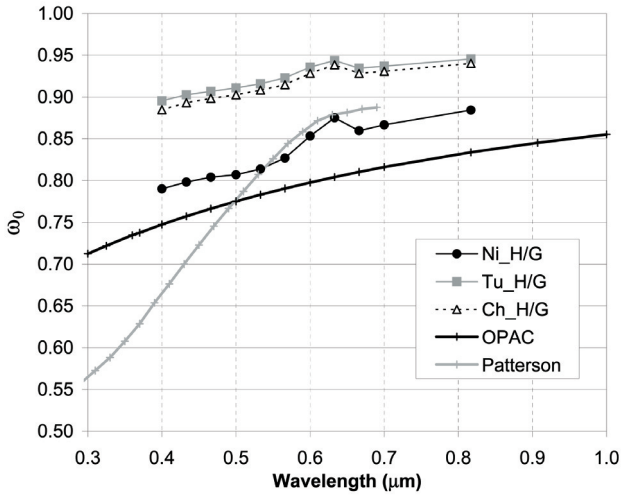

Figure 12. Single-scattering albedos as a function of wavelength computed for Niger, Tunisia, and China wind tunnel aerosol samples by taking into account all relevant data obtained in this study. Single-scattering albedos calculated with the OPAC and *Patterson et al.* [1977] refractive indices are also shown for comparison.

[78] 2. Free iron takes between 25% and 75% of the total iron mass depending on a particular sample. The free iron content (expressed as a mass percentage) shows more variability than the total iron content does. We did not find a clear relationship between variability of free iron and either dust origin or aging, though they both may be a factor. Indeed, the linkage between soil and aerosol iron content is not simple and needs to be further explored. The free iron content and free-Fe/Al ratios are larger in coarse particles compared to fine ones.

[79] 3. In each sample, we found more goethite than hematite. This stresses the need to include goethite in dust modeling.

[80] 4. Measurements of iron content and mineralogy were used to reconstruct the iron oxide–clay aggregates. In particular, a volume fraction of iron oxide in aggregates was computed in several different ways to investigate how iron oxide characteristics (free versus total iron, goethite versus hematite, and bulk versus size-segregated free iron) affect the effective refractive indices of aggregates and their optical properties. By considering the mixtures of iron oxide–clay aggregates with other light nonabsorbing species that were constrained by the elemental analysis data, the effects of iron oxide characteristics on the optical properties of regional dust mixtures were investigated.

[81] We found that the real part of the effective refractive index of aggregates depends on the mineralogy of both iron oxides (hematite versus goethite) and clays (illite versus kaolinite), while the imaginary part is controlled mainly by the volume fraction of iron oxides. The extinction coefficient of aggregates depends little on their mineralogy.

[82] 5. Although a substantial body of data on total iron exists, considering total iron in modeling the optical properties results in a lower single-scattering albedo of iron oxide–clay aggregates compared to that predicted with free iron. Furthermore, variability of the free iron content can be larger than that of total iron. Given that it is a key factor in determining how much dust can absorb, new data on free iron content in regional dust are urgently needed.

[83] 6. The variability of free iron content not only affects the single-scattering albedo of aggregates but also ω_0 of their external mixtures with nonabsorbing minerals. In addition, regional differences in relative abundance of aggregates and other minerals contribute to differences in ω_0 between regional dust samples.

[84] 7. We found large differences in the single-scattering albedo calculated for the fine and coarse modes. They are due to both size and the fact that coarse aggregates contain more iron oxides than fine ones.

[85] 8. Considering hematite or goethite in optical calculation leads to large differences, especially in the wavelength dependence of ω_0. New techniques will need to be developed to quantify the fraction of these species in aggregates.

[86] Overall, we conclude that information on the size-resolved content of free iron and a fraction of hematite and goethite in aggregates will need to be known on a regional basis to improve the prediction of the single-scattering albedo at the solar wavelengths and hence the radiative effects of atmospheric mineral dust. Given the diverse dust sources, more realistic representation of regional dust properties will be of great importance to both climate studies and various remote sensing applications.

[87] **Acknowledgments.** The authors are grateful to all of the personnel who were involved in wind tunnel experiments. Special thanks are due to S. C. Alfaro and M. Maillé for making wind tunnel measurements successful. We also thank the Institut de Minéralogie et de Physique des Milieux Condensés (IMPMC) for providing access to a spectrophotometer for measurements of diffuse reflectances. This work was partially supported by the Office of Naval Research and the Programme National de Recherche Sols et Erosion ("Statuts du fer dans les aérosols désertiques en relation avec les sols parents et l'intensité de l'érosion éolienne").

References

Alfaro, S. C., and L. Gomes (1995), Improving the large-scale modeling of the saltation flux of soil particles in presence of nonerodible elements, *J. Geophys. Res.*, *100*, 16,357–16,366.

Alfaro, S. C., and L. Gomes (2001), Modeling mineral aerosol production by wind erosion: Emission intensities and aerosol size distributions in source areas, *J. Geophys. Res.*, *106*, 18,075–18,084.

Alfaro, S. C., A. Gaudichet, L. Gomes, and M. Maillé (1998), Mineral aerosol production by wind erosion: Aerosol particle sizes and binding energy, *Geophys. Res. Lett.*, *25*, 991–994.

Alfaro, S. C., et al. (2003), Chemical and optical characterization of aerosols measured in spring 2002 at the ACE-Asia supersite, Zhenbeitai, China, *J. Geophys. Res.*, *108*(D23), 8641, doi:10.1029/2002JD003214.

Alfaro, S. C., S. Lafon, J. L. Rajot, P. Formenti, A. Gaudichet, and M. Maillé (2004), Iron oxides and light absorption by pure desert dust: An experimental study, *J. Geophys. Res.*, *109*, D08208, doi:10.1029/2003JD004374.

Anderson, T. L., S. J. Masonis, D. S. Covert, N. C. Ahlquist, S. G. Howell, A. D. Clarke, and C. S. McNaughton (2003), Variability of aerosol optical properties derived from in situ aircraft measurements during ACE-Asia, *J. Geophys. Res.*, *108*(D23), 8647, doi:10.1029/2002JD003247.

Arimoto, R., W. Balsam, and C. Schloesslin (2002), Visible spectroscopy of aerosol particles collected on filters: Iron-oxide minerals, *Atmos. Environ.*, *36*, 89–96.

Baize, D. (2000), *Guide des Analyses en Pédologie*, 257 pp., INRA, Paris.

Bedidi, A., and B. Cervelle (1993), Light scattering by spherical particles with hematite- and goethite-like optical properties: Effect of water impregnation, *J. Geophys. Res.*, *98*, 11,941–11,952.

Caquineau, S. (1997), Les sources des aerosols sahariens transportés au dessus de l'Atlantique tropical Nord: Localisation et caractéristiques minéralogiques, Ph.D. thesis, 181 pp., Univ.é Paris 12, Val-de-Marne, France.

Caquineau, S., A. Gaudichet, L. Gomes, M.-C. Magonthier, and B. Chatenet (1998), Saharan dust: Clay ratio as a relevant tracer to assess the origin of soil-derived aerosols, *Geophys. Res. Lett.*, *25*, 983–986.

Caquineau, S., A. Gaudichet, L. Gomes, and M. Legrand (2002), Mineralogy of Saharan dust transported over the northwestern tropical Atlantic Ocean in relation to source regions, *J. Geophys. Res.*, *107*(D15), 4251, doi:10.1029/2000JD000247.

Chester, R., H. Elderfield, J. J. Griffin, L. R. Johnson, and R. C. Padgham (1972), Eolian dust along the eastern margins of the Atlantic Ocean, *Mar. Geol.*, *13*, 91–105.

Chester, R., G. G. Baxter, A. K. A. Behairy, K. Connor, D. Cross, H. Elderfield, and R. C. Padgham (1977), Soil-sized eolian dusts from the lower troposphere of the eastern Mediterranean sea, *Mar. Geol.*, *24*, 201–217.

Chiapello, I., G. Bergametti, B. Chatenet, P. Bousquet, F. Dulac, and E. Santos Soares (1997), Origins of African dust transported over the northeastern tropical Atlantic, *J. Geophys. Res.*, *102*, 13,701–13,709.

d'Almeida, G. A., P. Koepke, and E. P. Shettle (1991), *Atmospheric Aerosols: Global Climatology and Radiative Characteristics*, 561 pp., A. Deepak, Hampton, Va.

Deer, W. A., R. A. Howie, and J. Zussman (1992), *An Introduction to the Rock-Forming Minerals*, 696 pp., Addison-Wesley, Boston, Mass.

Dubovik, O., B. Holben, T. F. Eck, A. Smirnov, Y. J. Kaufman, M. D. King, D. Tanré, and I. Slutsker (2002), Variability of absorption and optical properties of key aerosol types observed worldwide locations, *J. Atmos. Sci.*, *59*, 590–608.

Elichegaray, C., A. Dutot, B. Grubis, and R. Vie Le Sage (1981), Dosage par fluorescence X des aérosols atmophériques: Détermination des facteurs de correction, *Analusis*, *9*, 492–497.

Eltayeb, M. A. H., J. Injuk, W. Maenhaut, and R. E. Van Grieken (2001), Elemental composition of mineral aerosol generated from Sudan Sahara sand, *J. Atmos. Chem.*, *40*, 247–273.

Falkovich, A. H., E. Ganor, Z. Levin, P. Formenti, and Y. Rudich (2001), Chemical and mineralogical analysis of individual mineral dust particles, *J. Geophys. Res.*, *106*, 18,029–18,036.

Faye, G. H. (1968), The optical spectra of six coordinate sites in chlorite, biotite, phlogopite and vivianite: Some aspects of pleochroism in the sheet silicates, *Can. Mineral.*, *9*, 403–425.

Formenti, P., et al. (2001), Physical and chemical characteristics of aerosols over the Negev (Israel) during summer 1996, *J. Geophys. Res.*, *106*, 4871–4890.

Gao, Y., Y. J. Kaufman, D. Tanré, D. Kolber, and P. G. Falkowski (2001), Seasonal distributions of the aeolian iron fluxes to the global ocean, *Geophys. Res. Lett.*, *28*, 29–32.

Glaccum, R. A., and J. M. Prospero (1980), Saharan aerosols over the tropical north Atlantic—Mineralogy, *Mar. Geol.*, *37*, 295–321.

Gomes, L., and D. A. Gillette (1993), A comparison of characteristics of aerosol from dust storms in central Asia with soil-derived dust from other regions, *Atmos. Environ., Part A*, *27*, 2539–2544.

Gomes, L., G. Bergametti, F. Dulac, and U. Ezat (1990), Assessing the actual size distribution of atmospheric aerosols collected with a cascade impactor, *J. Aerosol Sci.*, *21*, 47–59.

Greenland, D. J., J. M. Oades, and T. W. Sherwin (1968), Electron-microscope observations of iron oxides in some red soils, *J. Soil Sci.*, *19*, 123–126.

Herrmann, L., K. Stahr, and R. Jahn (1999), The importance of source region identification and their properties for soil-derived dust: The case of Harmattan dust sources for eastern West Africa, *Contrib. Atmos. Phys.*, *72*, 141–150.

Hess, M., P. Koepke, and I. Schult (1998), Optical properties of aerosols and clouds: The software package OPAC, *Bull. Am. Meteorol. Soc.*, *79*, 831–844.

Intergovernmental Panel on Climate Change (2001), *Climate Change 2001: The Scientific Basis, Contribution of Working Group I to the Third Assessment Report of the Intergovernmental Panel on Climate Change*, edited by J. T. Houghton et al., 881 pp., Cambridge Univ. Press, New York.

Jepson, W. B. (1988), Structural iron in kaolinites and in associated ancillary minerals, in *Iron in Soils and Clay Minerals*, edited by J. W. Stucki et al., pp. 467–536, Springer, New York.

Karickhoff, S. W., and G. W. Bailey (1973), Optical absorption spectra of clay minerals, *Clays Clay Min.*, *21*, 59–70.

Kaufman, Y. J., D. Tanre, O. Dubovik, A. Karnieli, and L. A. Remer (2001), Absorption of sunlight by dust as inferred from satellite and ground-based remote sensing, *Geophys. Res. Lett.*, *28*, 1479–1482.

Lafon, S. (2004), Les oxydes de fer dans l'aérosol désertique en relation avec ses propriétés optiques: caractérisation physico-chimique de poussières minérales générées en soufflerie, Ph.D. thesis, 325 pp., Univ. é Paris 12, Val-de-Marne, Créteil, France.

Lafon, S., J. L. Rajot, S. C. Alfaro, and A. Gaudichet (2004), Quantification of iron oxides in desert aerosols, *Atmos. Environ.*, *38*, 1211–1218.

Mehra, O. P., and M. L. Jackson (1960), Iron oxide removal from soils and clays by a dithionite-citrate system buffered with sodium bicarbonate, *Clays Clay Min.*, *7*, 317–327.

Merrill, J., E. Arnold, M. Leinen, and C. Weaver (1994), Mineralogy of aeolian dust reaching the North Pacific Ocean: 2. Relationship of mineral assemblages to atmospheric transport patterns, *J. Geophys. Res.*, *99*, 21,025–21,032.

Mori, I., M. Nishikawa, T. Tanimura, and H. Quan (2003), Change in size distribution and chemical composition of kosa (Asian dust) aerosol during long-range transport, *Atmos. Environ.*, *37*, 4253–4263.

Patterson, E. M., D. A. Gillette, and B. H. Stockton (1977), Complex index of refraction between 300 and 700 nm for Saharan aerosols, *J. Geophys. Res.*, *82*, 3153–3160.

Rajot, J. L. (2001), Wind blown sediment mass budget of Sahelian village land units in Niger, *Bull. Soc. Geol. France*, *172*, 523–531.

Reid, J. S., et al. (2003), Comparison of size and morphological measurements of coarse mode dust particles from Africa, *J. Geophys. Res.*, *108*(D19), 8593, doi:10.1029/2002JD002485.

Scheinost, A. C., A. Chavernas, V. Barron, and J. Torrent (1998), Use and limitations of second-derivative diffuse reflectance spectroscopy in the visible range to identify and quantify Fe oxide minerals in soils, *Clays Clay Min.*, *46*, 528–536.

Seinfeld, J. H., and S. N. Pandis (1998), *Atmospheric Chemistry and Physics: From Air Pollution to Climate Change*, 1326 pp., John Wiley, Hoboken, N. J.

Sherman, D. M., and T. D. Waite (1985), Electronic spectra of Fe3+ oxides and oxide hydroxides in the near IR to near UV, *Am. Mineral.*, *70*, 1262–1269.

Sokolik, I. N., and O. B. Toon (1996), Direct radiative forcing by anthropogenic airborne mineral aerosols, *Nature*, *381*, 681–683.

Sokolik, I. N., and O. B. Toon (1999), Incorporation of the mineralogical composition into models of the radiative properties of mineral aerosol from UV to IR wavelengths, *J. Geophys. Res.*, *104*, 9423–9444.

Sokolik, I. N., D. Winker, G. Bergametti, D. Gillette, G. Carmichael, Y. Kaufman, L. Gomes, L. Schuetz, and J. Penner (2001), Introduction to special section on mineral dust: Outstanding problems in quantifying the radiative impact of mineral dust, *J. Geophys. Res.*, *106*, 18,015–18,028.

Sumner, M. E. (1963), Effect of iron oxides on positive and negative charges in clays and soils, *Clay Min. Bull.*, *5*, 218–226.

World Climate Program (1983), WMO report of the Experts' Meeting on Aerosols and Their Climatic Effects, *Rep. WCP-55*, Geneva, Switzerland.

Zhang, X. Y., S. L. Gong, R. Arimoto, Z. X. Shen, F. M. Mei, D. Wang, and Y. Cheng (2003), Characterization and temporal variation of Asian dust aerosol from a site in the northern Chinese deserts, *J. Atmos. Chem.*, *44*, 241–257.

S. Caquineau, Institut de Recherche pour le Développement, UR Paleotropique, 32, Rue Henri Varagnat, F-93143 Bondy cedex, France.

A. Gaudichet, Laboratoire Interuniversitaire des Systèmes Atmosphériques, UMR-CNRS 7583, Université Paris 12, 61 avenue du Général de Gaulle, F-94010 Créteil, France.

S. Lafon and I. N. Sokolik, School of Earth and Atmospheric Sciences, Georgia Institute of Technology, 311 Ferst Drive, Atlanta, GA 30332-0340, USA. (sandra.lafon@eas.gatech.edu)

J. L. Rajot, Institut de Recherche pour le Développement, UR 049, BP 11416, Niamey, Niger.